Spatial transcriptomics in adult *Drosophila* reveals new cell types in the brain and identifies subcellular mRNA patterns in muscles

Jasper Janssens[1,3], Pierre Mangeol[4,#], Nikolai Hecker[1,2,3,#], Gabriele Partel[1,2,3,#], Katina Spanier[1,2,3], Joy Ismail[1,3], Gert Hulselmans[1,2,3], Stein Aerts[1,2,3,*], Frank Schnorrer[4,*]

[1] VIB-KU Leuven Center for Brain and Disease Research, KU Leuven, 3000 Leuven, Belgium.

[2] VIB Center for AI & Computational Biology, KU Leuven, 3000 Leuven, Belgium.

[3] Laboratory of Computational Biology, Department of Human Genetics, KU Leuven, 3000 Leuven, Belgium.

[4] Aix Marseille University, CNRS, IBDM, Turing Centre for Living Systems, 13288 Marseille, France.

[#] Co-2nd authors
[*] Co-last authors

Correspondence:
stein.aerts@kuleuven.be
frank.schnorrer@univ-amu.fr

Keywords: spatial transcriptomics, *Drosophila*, brain, muscle, FISH, mRNA localization, single-cell atlas;

Recently, we have achieved a significant milestone with the creation of the Fly Cell Atlas. This single-nuclei atlas encompasses the entire fly, covering the entire head and body, in addition to all major organs. This atlas catalogs hundreds to thousands of cell types, of which we annotated 250. This still leaves many clusters to be fully characterized, in particular in the brain. Furthermore, with single-nuclei sequencing, all information about the spatial location of the cells and of the mRNAs within these cells is lost. Here, we provide a solution to this problem. In a proof of concept study, we have applied spatial transcriptomics using a selected gene panel to pinpoint the locations of 150 mRNA species in the adult fly. This enabled us to map unknown cell types identified in the Fly Cell Atlas to their spatial locations in the brain. Additionally, spatial transcriptomics discovered interesting principles of mRNA localization in large crowded muscle cells that may spark future mechanistic investigations. Furthermore, we present a set of computational tools that will allow for easier integration of spatial transcriptomics and single-cell datasets.

Introduction

Single-cell technologies have revolutionized biological research, allowing researchers for the first time to study complex tissues with unprecedented resolution (Klein et al., 2015), leading to the creation of tissue-specific atlases (Schaum et al., 2018; The Tabula Sapiens consortium, 2022). However, upon tissue dissociation into single cells, all spatial information of the cell in the organism and of the mRNAs within the cell is lost, since all data of the cell are compressed into one multidimensional data point. This is a significant drawback, as the localization of a cell type within a tissue can inform about the function of this cell (Tomancak et al., 2002). Furthermore, many mRNAs show subcellular localization patterns that may have functional roles (Jambor et al., 2015; Lécuyer et al., 2007).

This loss of information can be circumvented using spatially resolved transcriptomics (SRT). In SRT, spatial information of the RNA species is determined either through the use of spatially localized barcoded DNA arrays with or without the use of microfluidics, followed by sequencing (Rodriques et al., 2019; Wang et al., 2022), or by imaging using fluorescence in situ hybridisation (FISH) methods. While barcoded sequencing approaches allow unbiased mapping of all transcripts, their spatial resolution is, in general, lower (Moses & Pachter, 2022). FISH identifies the position of each RNA molecule independently at a high spatial resolution, but is limited in throughput to a few genes. Recently, technical breakthroughs have been presented to increase the number of genes to several hundred through the use of barcoding (Chen et al., 2015; Eng et al., 2019; Lubeck et al., 2014; Zhang et al., 2021).

The adult fruit fly *Drosophila melanogaster* is a widely used model for cell biology, neurobiology, physiology and behavior (Sokolowski, 2001; Grenier & Leulier, 2020; Benton, 2022). The recent completion of the entire adult fly cell atlas (FCA) (Li et al., 2022), and the aging fly cell atlas (Lu et al., 2023) provided an in-depth annotation of various cell types, however without information about the localization of these cells or their mRNAs. In addition, several single-cell clusters were left unannotated although marker genes were identified.

Here we applied Molecular Cartography (Resolve Biosciences) to create a FISH-based spatial transcriptomics dataset of the entire head and body of adult *Drosophila melanogaster* flies. While embryonic development has already been studied using SRT (Wang et al., 2022), we present the first high-throughput single-molecule FISH-based SRT dataset of the various tissues of the adult fly. We compare the data with existing RNA atlases, using the spatial data to validate annotations in the body and identify unknown clusters in the brain. Furthermore, we use the data to reveal subcellular mRNA localization patterns in the flight muscle cells and regionalized RNA expression in the head. Expression patterns of 100 genes in the brain and 50 genes in the body can be visualized interactively using TissUUmaps (Solorzano et al., 2020) at www.spatialfly.aertslab.org.

Results

Creation of a spatial atlas of the entire fly body and its head

In analogy to the FCA strategy (Li et al., 2022), we intended to create a spatial atlas of the entire adult fly body and, additionally, of the head separately. Based on expression data from the FCA (Li et al., 2022), we selected 50 genes for the fly body samples, and 100 genes for the head samples. These genes were carefully chosen to label the most important known cell types of the adult fly, and to include some unknown ones, suggested from the atlas data (Table S1-S2, Fig. S1). This approach should allow us to separate the large heterogeneity of neurons in different populations. Adult fly samples were cryofrozen, sectioned, attached to slides and fixed (see Methods), after which they were profiled using Molecular Cartography (Resolve Biosciences) (Fig. 1a). Using this workflow we detected on average 190,622 mRNA molecules for the head samples (min=101,548, max=260,989), ranging from 106 (*Poxn*) to 185,820 (*trio*) per gene (Fig. S2a-b) and 1.5 million mRNA molecules for the body samples (min=1,448,593, max=1,727,479), ranging from 323 (*MsR1*) to 1,991,469 (*Act88F*) counts per gene used (Fig. S3a-b).

For the head samples, we aimed to image as many different neuronal populations as possible. Thus, we performed coronal sections at different depths in the head (n=13), covering anterior to posterior parts of the head (Fig. 1b, Fig. S2a,c). For the body samples, sagittal sections were performed through the middle of the animal (n=5) (Fig. 1c, Fig. S3a). These sagittal sections show some small differences in structures in the abdomen, but overall are very similar to each other, showing the reproducibility of our methods. In total, we analyzed 5 body sample sections from one adult male fly and found a high correlation between them (Fig. S3c, see Methods).

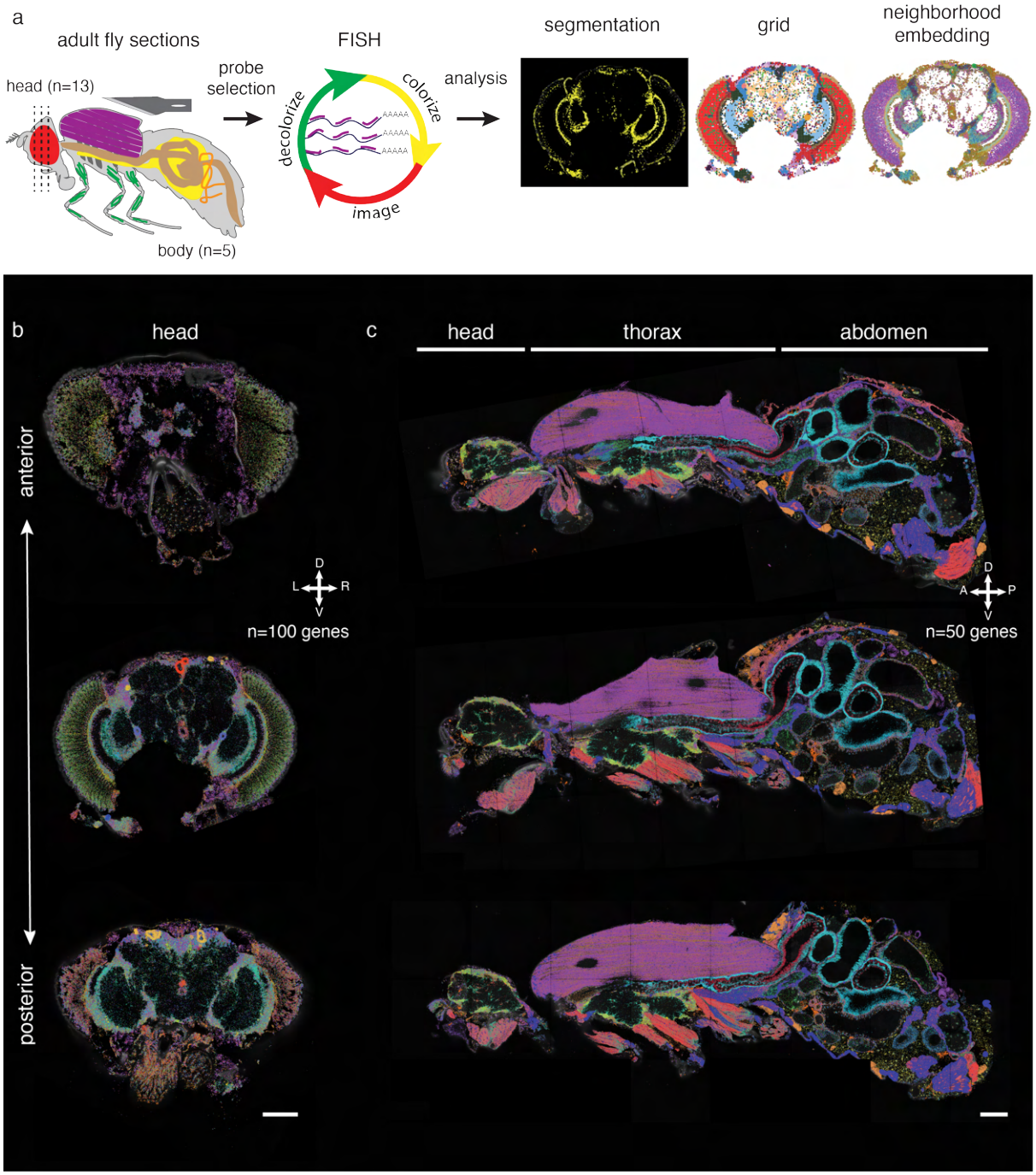

Figure 1. Principal workflow of the spatial fly atlas. *a) overview of the workflow: adult flies were sectioned, sections were analyzed with repetitive FISH and data were annotated using cell segmentation, clusterization (i.e. grid) and neighborhood embedding (Methods). b) Example data for adult head sections showing various positions in the brain along the anterior-posterior axis. c) Examples of male whole-body sections. mRNAs from each gene are represented in a different color. The combination of colors reveals the different cell types. Scale bars represent 100 µm.*

Spatial transcriptomics allows the identification of cell types in the body

The genes for the body datasets were selected to cover a wide range of different cell types. The expression of *elav* and *Syt1* is marking neurons, both in the central and peripheral nervous system at the expected locations (Fig. 2a). The glial marker *repo* shows the location of glial cells across the body (Fig. 2a). The expression of different trypsins is unique to the digestive

system. Interestingly, *alpha-* and *betaTrypsin* show distinct patterns, with *betaTrypsin* localized on the inner side of the gut, while *alphaTrypsin* is localized more distally, suggesting a subcellular localization of these trypsin isoform coding mRNAs to apical or basal regions of the gut enterocytes (Fig. 2a). Using the fat body marker *AkhR* and the oenocyte marker *FASN2*, different populations of fat tissue and oenocytes were identified in the abdomen of the fly at the expected locations. The hemocyte marker *Hml* shows distinct local enrichments in head, thorax and abdomen (Fig. 2a). In addition, *LanB1*, which codes for LamininB1, an important component of the extracellular matrix present around many tissues (Yarnitzky & Volk, 1995), is widely produced in different cell types and not only in hemocytes. While co-expression of *LanB1* with *Hml* in hemocytes is detected as reported (Matsubayashi et al., 2017) (15.5%) (Fig. 2a), surprisingly most of *LanB1* overlaps with epithelial cells (*grh* (13.4%) and *pain* (28.0%)) or muscle cells (*Mlp84B* (40.9%) and *Mp20* (25.4%) (see Methods)). Next, we used *esg* to mark adult stem cell populations. The expression of *esg* in our sections is mostly limited to the gut, matching its reported expression in the intestinal stem cells (Jiang & Edgar, 2011) and the somatic cyst stem cells (Sênos Demarco et al., 2022) (Fig. 2a). Furthermore, *Mhc* and *sls* were used to label all muscle cells, while *TpnC4* and *Act88F* allowed to specifically label the indirect flight muscles (IFM) (Fig 2a). Finally, we used *grh, hth, svp* and *pain* to identify epithelial cells and their subtypes. Together, these data show that our spatial transcriptomics data can identify the spatial location of most known large classes of cell types of the adult fly and also identify unexpected subcellular mRNA localizations in some cell types.

Molecular Cartography is highly specific

Many marker genes used in this study are well characterized and known to be highly specific for one particular cell type or present in one body location. Hence, their expression can be used to estimate the specificity of the mRNA detection method and determine false-positive rates of mRNA spots. For this specificity analysis, we chose to work with marker genes linked to muscle cells. We used the expression of *Act88F* and *TpnC4*, both of which are almost exclusively expressed in the indirect flight muscles present only in the thorax (and possibly in muscles around the ejaculatory bulb) (Fyrberg et al., 1983; Agianian et al., 2004; Sarov et al., 2016). We segmented the flight muscles (Fig. 2a) and calculated the percentage of marker genes detected in the segmented area compared to the entire imaged area. We find that 99.1% of *TpnC4* and 99.6% of *Act88F* are specifically expressed in their expected regions (Fig. 2a). Signals outside of these regions are negligible. This highlights the specificity of the transcriptomics method and the reliability of detected mRNA signals.

Building a spatial tissue atlas of the fly body

Having shown the specificity of our method, we wanted to use the combinatorial power of our data to assign cell type identities more reliably. Often, cell types can only be reliably identified by a combination of several marker genes. Therefore, we investigated co-expression signatures of known cell type marker genes in the spatial transcriptomics data. This may also help identify more rare cell types or specific cell states. To implement this idea on our spatial data, we computationally assigned every mRNA molecule to a 5 µm by 5 µm square in a square-grid fashion. All squares in this grid were then scored for mRNA signatures of different cell classes (Fig. 2b). Next, we assigned every square to the cell class for which they showed the highest signal (see Methods). This signature-based method annotated all major cell types

or tissues of the adult reliably, including muscles, neurons, glia, fat and epithelial cells, oenocytes and the male reproductive organ (Fig 2b). This analysis also enabled the identification of cell populations with more sparse gene expression like the heart (combination of *Hand* and *tin*) or the male reproductive tract (combination of *Awh*, *eyg* and *svp*). In conclusion, the major cell types of the adult fly could be localized using the power of combining mRNA localizations of different marker genes and their spatial proximity.

As a next step, we aimed to assign cell type locations without prior knowledge of their markers. To do so, we used all 132,642 different squares from each of the 5 body samples and performed clustering based on the counts of the 50 genes analyzed (see Methods). This led to the identification of 142 clusters that we visualized as a UMAP plot, separating muscle from neuronal and epithelial cells (Fig. 2c). The spatial visualization of this unsupervised analysis of cell types confirmed our previous supervised annotation of cell types based on gene signatures (Fig. 2d). In addition, it showed an unexpected presence of multiple clusters in the large flight muscle cells, suggesting subcellular mRNA patterns. These results underscore the power of assigning the spatial location of adult *Drosophila* cell types with spatial transcriptomics.

Finally, we looked at the expression of genes in one particular organ to identify its different cell types. In the FCA, we had previously identified *Awh*, *eyg* and *nAChRalpha1* to label the male accessory gland main cells (Fig. 2e). Our SRT data confirm this co-expression, showing the labeling of the main gland cells in the abdomen (Fig. 2f). Next, we performed a more detailed comparison of our SRT data with the FCA scRNA-seq. We calculated the correlation between genes in both SRT and scRNA-seq to find if co-expression is maintained in both datasets (see Methods). In general, gene-gene correlations between SRT and scRNA-seq match significantly ($r=0.69$, $p<1e-100$), with no major disagreements between the two (Fig. S4a-b). This indicates that in general SRT data corroborate results obtained from scRNA-seq. To study gene-gene relations in more detail, we devised an algorithm that calculates for each gene its colocalization with other genes (see Methods) (Fig. S5a-b). This colocalization matrix was then clustered to find groups of genes that are co-expressed. These groups match with the major cell types, while also highlighting genes expressed in male reproduction to be specifically localized. In addition, this analysis method grouped neuronal and muscular genes into the same cluster, consistent with the close proximity between these two cell types (Fig S5c).

In conclusion, cell-type-specific marker genes can be used for the unambiguous identification of cell types in SRT data. Furthermore, we highlight both high specificity and high reproducibility across adult fly body sections in our data. Together, this dataset represents the first SRT dataset for the adult fly body.

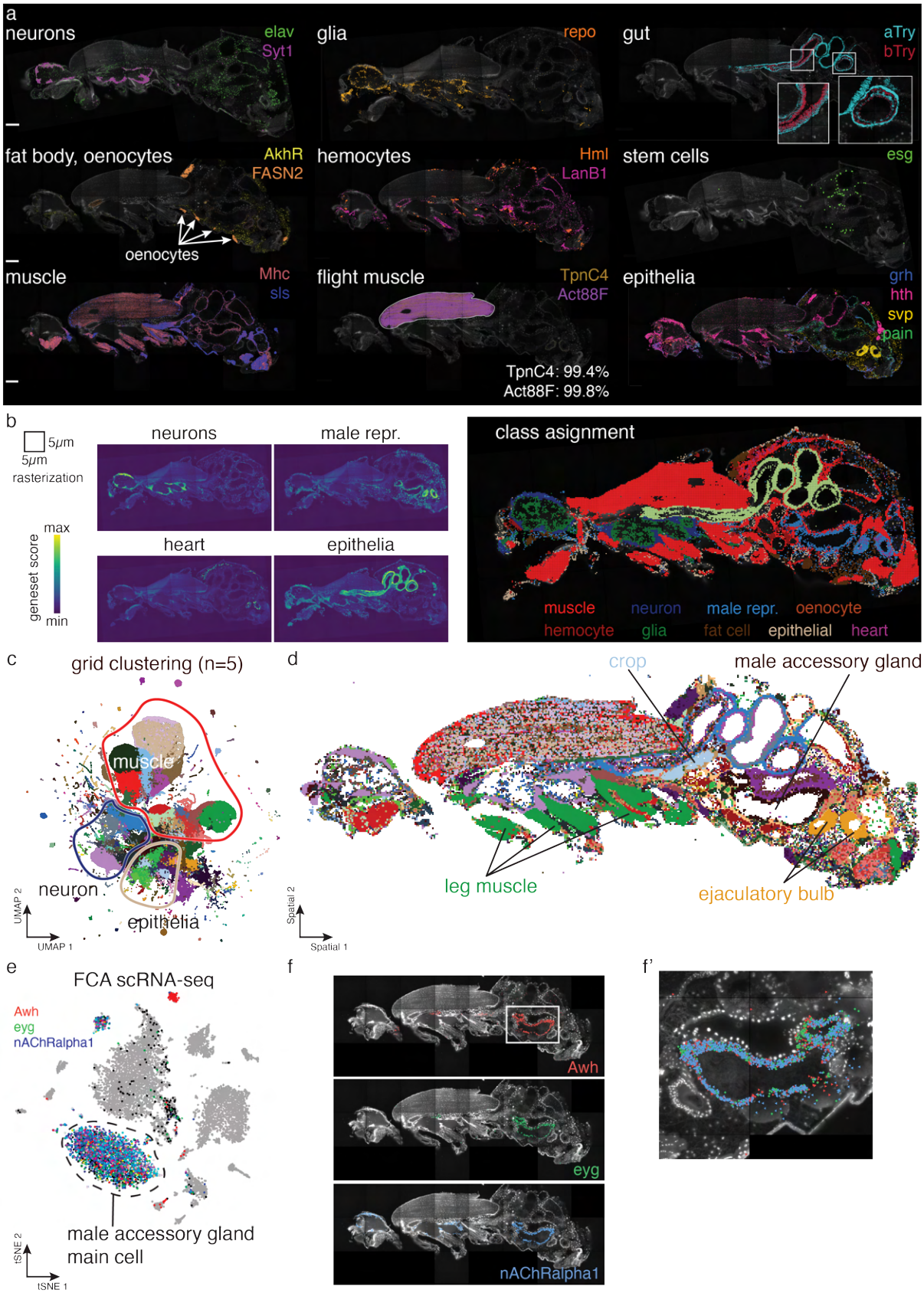

Figure 2. Adult body cell types. *a) Major cell types of adult males identified by marker genes. Scale bars represent 100 μm. Inset for gut shows zoom-ins of different regions. Inset for flight muscle, shows the percentage of marker gene molecules detected within the outlined area. b) Gene set scores for different main classes of cell types. Quantified using 5 μm x 5 μm grid.*

Class assignment shown on the right, based on maximum score. Genes used: Neurons: elav, Syt1, Sh, acj6, ey, VAChT, Gad1, VGlut, nAChRalpha7; male repr.: Awh, eyg, svp; epithelia: grh, alphaTry, betaTry, hth; heart: tin, Hand. c) UMAP showing clustering of 5 µm x 5 µm grid spots. d) Spatial location of grid clusters. e) tSNE from male accessory glands from FCA showing expression of marker genes for main gland cells. f) Spatial FISH of the main gland cells marker genes highlights a defined population. Detailed view shown in f'.

Subcellular localization of mRNA in muscle cells

Unsupervised clustering revealed the presence of multiple spatial subclusters in the muscles, especially in the indirect flight muscle (Fig. 2c, d), suggesting transcriptional heterogeneity or subcellular mRNA localization. Such mRNA localization could result from directed mRNA transport or anchoring (Martin & Ephrussi, 2009). To investigate this interesting observation in more detail, we segmented our sections containing the three main types of adult muscles: head, leg and indirect flight muscles. Muscle cells represent by far the largest cells in the body, forming polynucleated syncytia, with the indirect flight muscles containing more than five hundred nuclei (Chaturvedi et al., 2017; Kaya-Çopur et al., 2021). These nuclei are distributed in specific patterns depending on the muscle fiber-type. In tubular muscle fibers found in the head or the legs, the nuclei are located in the center of the muscle, in a row surrounded by the contractile myofibrils. In the fibrillar indirect flight muscles, the nuclei are arranged in multiple rows located between the contractile myofibril bundles (Luis & Schnorrer, 2021; Schönbauer et al., 2011). Hence, the nuclei are equally distributed along the length of the large 1 mm long flight muscle fibers (Spletter et al., 2018). This organization has been proposed to optimize the distribution of mRNAs by minimizing transport distances (Bruusgaard et al., 2003). Misalignment of the nuclei has been linked to a variety of severe myopathies in humans (Folker & Baylies, 2013). While snRNA-seq allows studying of potentially different types of nuclei in the muscle, FISH has been proposed as a method to study and describe mRNA localization in muscle fibers in earlier studies (Denes et al., 2021; Pinheiro et al., 2021).

Amongst the 50 genes we had selected were six genes that code for sarcomere protein components, four of which are specifically expressed in different muscle groups, *Act88F* and *TpnC4* in indirect flight muscles, *Act79B* and *TpnC41C* in leg muscles. Our SRT data verified these spatially distinct expression patterns, again reassuring the specificity of our method (Fig. 3a).

By analyzing the subcellular localization of the sarcomere protein coding mRNAs in detail we noticed that mRNAs of the pan-muscular gene *sls*, show a striking proximity to the muscle nuclei marked by DAPI (Fig. 3b). To quantify this proximity and the subcellular patterns accurately, we first identified each nucleus by segmenting the DAPI signal and then calculated the position of each mRNA molecule in the muscle cell and its distance to the closest nucleus (see Methods, resolution is 0.136 µm). This identified genes, whose mRNAs are nuclei-enriched (*sls*) and nuclei-depleted (*TpnC4*) (Fig. 3b-d, Fig. S6a). We found a similar difference in leg and head muscles with *sls* staying in proximity or within the nuclei, in contrast to *TpnC41C* located at a distance (Fig. S6b-c). Previously, mRNA distributions quantified in *in vitro* grown mammalian skeletal muscles were linked to mRNA sizes, with large mRNAs spreading further from the nuclei than small mRNAs (Pinheiro et al., 2021). This does not appear to be the general rule for *Drosophila* muscles as *sls* mRNAs are much longer (isoform

lengths: 15,263 - 56,489 nt) than *TpnC4* (longest is 859 nt) or TpnC41C mRNAs (longest is 1880 nt).

Even more striking than the sole distance from the nuclei is that mRNAs from particular genes, most prominently *Act88F* in flight muscles, are concentrated in longitudinal stripes in the inter-myofibril space, where most nuclei, endoplasmic reticulum and Golgi are located (Fig. 3d). mRNAs from *TpnC4* or *Mhc* are enriched in the complementary stripes at the location of the myofibrils and mitochondria (Fig. 3d), resulting in a spatial division of the flight muscles that correlates with their intracellular architecture (Avellaneda et al., 2021; Luis & Schnorrer, 2021). A similar division was found in leg muscles, with central stripes of *Act79B* mRNA close to the nuclei and *Mhc* as well as *TpnC41C* in the myofibril regions (Fig. S6b). These findings underscore the power of SRT to identify unexpected mRNA localization patterns that in particular in the large muscle cells may be of functional relevance.

Another interesting question that SRT may help to answer is whether all nuclei in a large flight muscle fiber follow the same transcriptional program. The FCA data did not reveal an obvious subdivision into different subclusters that demonstrated transcriptional heterogeneity (Li et al., 2022). Hence, we were surprised to find that the nuclei located at the anterior and posterior ends of the flight muscle fibers, facing the muscle-tendon attachment sites, show a concentration of *sls* mRNA compared to the other nuclei (Fig. 3a, e, Fig. S6a). Of the 50 genes tested, *sls* is the only gene that showed such a distinct mRNA localization pattern.

To conclude, we found three main types of mRNA localization in the indirect flight muscle: nuclei-enriched patterns, complementary striped bands and concentrations at the terminal nuclei close to the muscle attachment sites. To our knowledge, none of these patterns had been identified before.

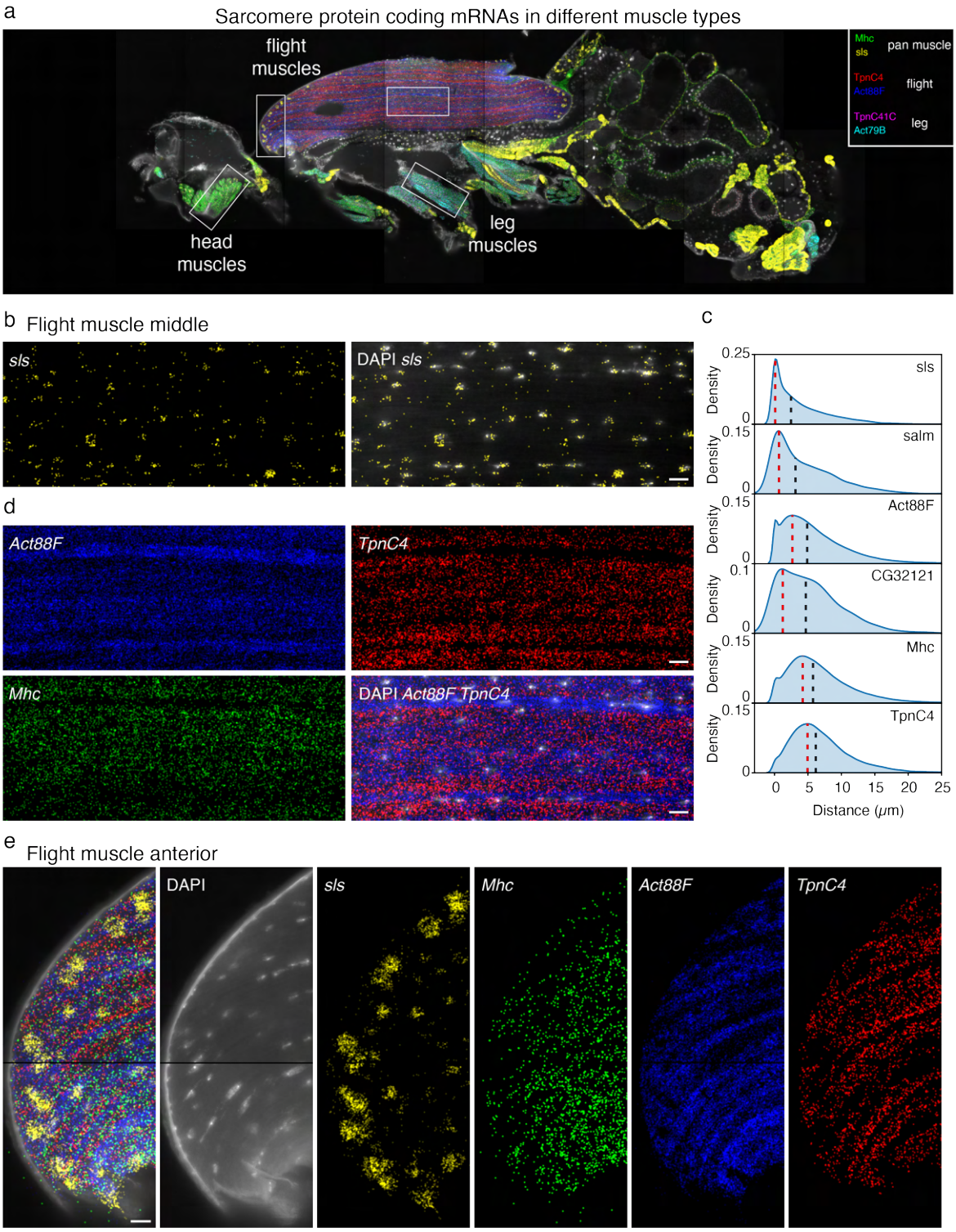

Figure 3. Molecular Cartography shows subcellular mRNA localization*. a) Molecular Cartography visualization of marker genes of muscle subtypes. White boxes mark zoom-in regions shown in (b, d, e, and Fig. S6). b) Zoom-in on flight muscle showing colocalization of sls mRNA and DAPI stained nuclei. c) Density plots showing the distance of each mRNA molecule to its nearest nucleus. Red dotted lines mark the peak density, black dotted lines the median distance. d) Zoom-in on flight muscle showing striped patterns of Act88F, Mhc and TpnC4 mRNA localization. e) Zoom-in on anterior flight muscle. Anterior nuclei show increased expression of sls, while patterns of Act88F, Mhc and TpnC4 are maintained. Scale bar in (a) represents 100 μm, scale bars in (b, d and e) represent 10 μm.*

Spatial transcriptomics allows the localization of cell types in the head and brain

To investigate the localization of cell types in the adult *Drosophila* head, we took 13 sections of different fly heads sectioned across the longitudinal direction, covering most regions of the fly head. The diversity between sections originating from different brain regions is represented by lower correlations between the samples (Fig. S2c). Using the marker genes *para* (neurons), *alrm* (astrocytes) and *ninaC* (photoreceptors), we were able to annotate different classes of cells (Fig. 4a). *ninaE*, a second photoreceptor marker was too highly expressed, leading to optical crowding and thus was removed from the analysis.

To look at cell types, we made use of our annotated scRNA-seq atlas of the fly brain (Davie et al., 2018; Li et al., 2022; Pech et al., 2023). First, we checked the expression of *C15*, *acj6*, *Oaz*, *caup* and *unpg*, known markers for olfactory projection neurons (OPNs). OPNs are neurons that relay information from the antennal lobe to downstream processing centers including the mushroom body and the lateral horn. The co-expression of all markers is only detected in the most anterior samples, corresponding to the location of OPN cell bodies (Fig. 4b), again showing the precision of our method. Next, we investigated the expression of markers for perineurial glia (*repo, moody*, *Indy*, *Vmat*), which form the blood-brain barrier (BBB) and find them at the periphery of the brain, the expected location (Fig. 4c).

We compared gene-gene relationships, by calculating gene-gene correlations in the spatial dataset and the single-cell dataset (Fig. S7a-b). In general, we find a strong match (r=0.68), but with several mismatches. While *pros-dati* co-expression is conserved between both modalities (Fig. S7c), co-expression of several other gene pairs is only detected in one modality (Fig. S7d-e). For example, we only find widespread expression of Vmat outside of the optic lobe in the BBB, far from the expected location of most dopaminergic neurons in the central brain (Fig. S7e). Additionally, *Vmat* expression does not overlap with DAPI-stained nuclei nor DAT (strong marker for dopaminergic neurons), suggesting an mRNA transport mechanism to locate selected mRNAs away from the cell body (Fig. S7e). Alternatively, glial nuclei, which are much smaller than neuronal nuclei (Mu et al., 2021), might not all be detected with our methodology. Similarly, the neuropeptides Ilp2 and Pdf show a weak overlap with the DAPI staining, instead forming patterns (Fig. S7e). Thus, SRT can recapitulate the location of known cell types in the fly brain by using established marker genes and additionally identify expression at novel locations for some of these.

Compared with other organs, the cell type diversity of the fly brain is extremely complex. A key challenge in scRNA-seq is the annotation of clusters to cell types. In our scRNA-seq dataset, there are 188 distinct clusters, of which only 83 are annotated today. Recent efforts to map the fly brain through EM and connectomics studies have identified 4,552 morphological cell types (Schlegel et al., 2023). SRT can provide a bridge between scRNA-seq studies and morphology-based studies. As such, it becomes possible to annotate unknown clusters based on the spatial localization of their marker genes. To pave the way towards such integration, we focused on unannotated clusters in our brain dataset. It is important to note that current neuronal nomenclature is based on neuropils (axons and dendrites) and not on the location of the neuronal nuclei. Therefore, we used the established neuropil nomenclature to describe

the location of the detected nuclei, but this does not necessarily mean that the axons of these cells also project there.

To identify the location of unknown clusters in the brain, we started with Fer1 expression, as it is a strong marker for cluster 120 in our scRNA dataset (Li et al., 2022). Using SRT we show conclusively that these cells are located in the central brain, in the ventral gnathal ganglion and saddle, and the superior intermediate protocerebrum (Fig. 4d). Similarly, we show that *AstC* expression (cluster 122) is limited to the dorsal part of the central brain, consistent with its expression in DN1 and DN3 neurons (Díaz et al., 2019) (Fig. 4d). Next, we investigated the expression of *otp* (clusters 30 and 62), which marks nuclei close to the lateral horn and the superior neuropils (Fig. 4e). Finally, we found the expression of *vg* (cluster 20) to be limited to the boundary region between the optic lobe (OL) and the central brain (CB) (Fig. 4e). These results confirm that combining scRNA-seq with SRT technologies can indeed identify defined locations of formerly unknown cell clusters in the fly brain.

Next, we wanted to find genes enriched to specific spatial locations in our brain SRT data. To do so, we assigned mRNA molecules to spots using a similar 5 µm resolution grid as done above for the body data. By performing unsupervised clustering using all mRNA localizations from all datasets together, we identified 23 clusters (Fig 4f). Consistent with our aim for sectioning along the brain's A-P axis, different slices display a different cluster composition (Fig. S7g). All neuronal clusters were selected using *para* expression and their location assigned them to the optic lobe (OL), the central brain (CB) or the retina (photoreceptor, PR). By performing differential expression between the domains, we identified enriched genes for each (Fig. 4g). As expected, photoreceptor genes such as *ninaC* and *lz* were strongly enriched in the retina. We found a large group of genes shared between the OL and CB, with upregulation of *pros* in the central brain and of *scro* in the OL (Fig. 4g). Analyzing the expression of these genes in different samples indeed confirmed a strong boundary in expression of these two transcription factors (Fig. 4h), corroborating earlier findings (Davie et al., 2018; Yoo et al., 2020). This shows that SRT alone can also identify specific markers for the major brain cell types, as shown above for the body, without any prior knowledge.

Finally, we wanted to compare gene expression between the dorsal and ventral parts of the brain, because a previous study had found that some scRNA-seq clusters in the fly brain could be divided into ventral *Wnt4* and dorsal *Wnt10* positive subclusters (Han et al., 2020; Özel et al., 2021). Using *Wnt4* and *Wnt10* mRNA localizations we could confirm these findings, and show that although expression is sparse, *Wnt4* and *Wnt10* mRNAs are strongly enriched in the ventral or dorsal regions of the brain, respectively (Fig. 4i).

Altogether, our SRT atlas of the fly brain shows that SRT data allows the identification of clusters and cell types. We also showed how SRT can be used to identify and localize unknown clusters of scRNA data, serving as a link between morphology data and single-cell data. Finally, SRT can be used for the discovery and confirmation of regional marker genes by performing region-based differential expression.

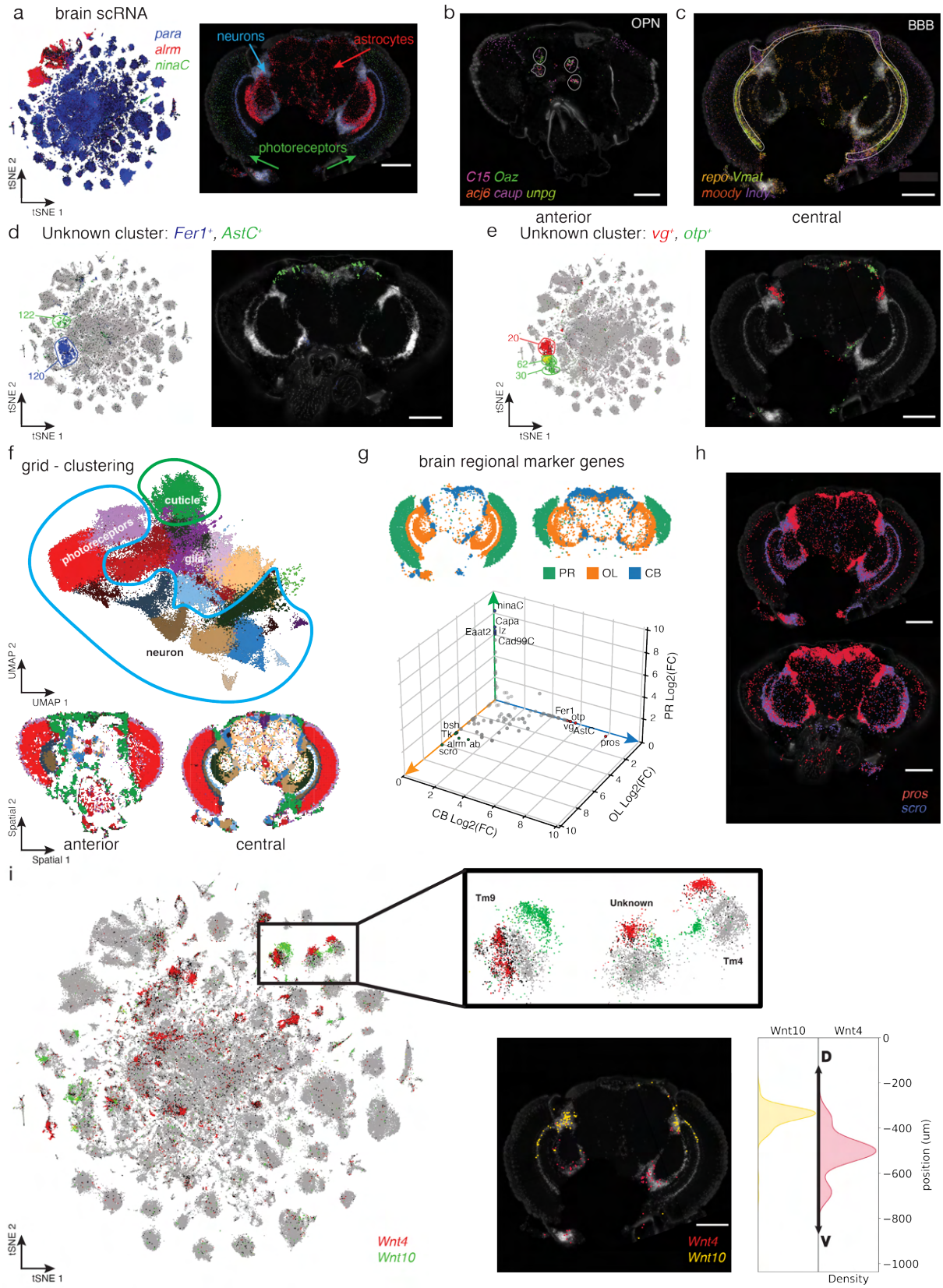

Figure 4. Adult head cell types. *a) tSNE showing expression of photoreceptor (ninaC), neuronal (para) and glial (repo) markers (left). Molecular Cartography of the same marker genes (right). b-c) Molecular Cartography of marker genes for olfactory projection neurons (OPN), in an anterior head slice (b) and of perineurial glia of the blood brain barrier (BBB) in a more central slice (c). d-e) Using Molecular Cartography to identify unknown clusters in*

scRNA-seq data. f) UMAP showing clustering of 5 µm x 5 µm grid spots (top). Spatial location of grid clusters (bottom). g) Differential expression of central brain, optic lobe and photoreceptor regions. h) Molecular Cartography of pros and scro. i) tSNE showing split in optic lobe clusters by expression of Wnt4 and Wnt10. Insert shows Molecular Cartography of Wnt4 and Wnt10, spatially localized in ventral and dorsal regions, respectively. Scale bars represent 100 µm.

Automated cell type annotation of SRT using scRNA-seq data

One of the key prospects for SRT, is to be able to identify unknown clusters and infer their spatial location. This requires the SRT data to be integrated with scRNA-seq data. Multiple methods have been developed for this purpose so far, including Tangram (Biancalani et al., 2021) and SpaGE (Abdelaal et al., 2020).

Here we used and compared three different approaches to represent SRT data: 5 µm-spaced grid rasterization, neighborhood embedding, and nuclei segmentation (Fig. 5a). The grid and neighborhood embedding are both spatially unaware of the cell's location. In the grid method, automatic segmentation takes place over the entire sample by grouping mRNA molecules together every 5 µm, while neighborhood embedding is segmentation-free and models every mRNA molecule independently. This makes it possible to also visualize spatial patterns at subcellular resolution, but leads to a very large dataset and hence is computationally heavy (Partel & Wählby, 2021). While the grid-based approach can be run in several hours, neighborhood embedding takes several days. Finally, we performed a segmentation method of the nuclei and assigned mRNA molecules to each nucleus. While this is the most intuitive method, several challenges occur in the fly head. To start, different densities of nuclei require imaging with different parameters to visualize both sparse and dense nuclei regions. In addition, the dense nuclei regions at the edge of the OL and CB are very difficult to segment with normal imaging techniques (Fig. 5b).

To compare different label transfer methods we applied lasso regression, Tangram and SPaGE. We found that regression-based integration in the grid method and SpaGE in the neighborhood embedding method are able to match the blood-brain barrier and the chiasm glia in the optic lobe very well, together with astrocytes and ensheathing glia in the central brain (Fig. 5c). In contrast, the nuclei segmentation method performs poorly for matching glial subtypes, since most of the glial nuclei are not detected, leading to the removal of most glial mRNAs (Fig. 5c). Therefore, we also ran Tangram on the grid-quantification, leading to the detection of different glial types (Fig. S8a-d). This shows a disadvantage of nuclei-aware methods compared to methods that take all mRNA spots into account.

In the OL, all methods can accurately identify neurons from the different layers. In the CB, both the grid-based and the segmentation methods are able to locate the peptidergic neurons (insulin-producing cells, Pdf-neurons) in the correct location, while neighborhood embedding fails to retrieve these (Fig. 5d, e). However, Tangram also labels some non-peptidergic segmented nuclei as insulin-producing unless thresholds for mapping scores are manually adjusted to reflect the different proportions of cell types that are present in the spatial transcriptomics data (Fig. S8e). In a more posterior central brain sample, nuclei segmentation

and grid methods are able to identify the Kenyon cells of the mushroom body. These are also found in the neighborhood embedding, but the signal is noisier (Fig. 5e). Neighborhood embedding likely performs poorly on cell types that are determined by high expression of only 1 gene (e.g. neuropeptides), since the neighborhood is not affected by this.

Finally, we investigated how the three approaches perform in linking unknown scRNA-seq clusters to spatial locations. Here we see that in the grid and neighborhood embedding methods, two unknown clusters are spatially localized, while the nuclei segmentation method can spatially localize four clusters (Fig. 5f). Cluster 20 which was marked by vg expression is found by each technique (Fig. 4e, Fig. 5f), same as cluster 79. Cluster 79 labels the outside of the retina, fitting with high expression of *Cpr72Ec*, a structural protein for the eye lens, which is expressed by interommatidial pigment cells (Stahl et al., 2017). In contrast to the other methods, Tangram detects a ventral-dorsal division in the retina, with cluster 15 matching to the dorsal part. This mapping is driven by the expression of *mirr*, a gene known to be expressed in the dorsal half of the eye (McNeill et al., 1997) (Fig. S8f). Tangram also maps cluster 69, mostly by expression of *caup*. Like its Iroquouis family member *mirr*, *caup* is detected in the dorsal half of the eye, but it shows additional expression in various locations in the central brain (Fig. S8g). Cluster 69 represents multiple subclusters in scRNA-seq data, and similarly it maps to multiple locations in the spatial data. A larger gene panel will help to dissect and locate the subclusters.

To conclude, we find that using a 5 µm by 5 µm grid leads to similar clustering results as performing a computationally heavy neighborhood embedding analysis. However, the neighborhood embedding does increase the resolution to single mRNA spots, leading to a better visualization and a higher spatial accuracy. The nuclei segmentation method is limited in the fly brain by the lack of resolution to identify the individual nuclei in very densely packed brain regions. While Tangram was the best method to identify unknown clusters, it also led to false-positive labeling of multiple cell types leading to the necessity of accurate thresholding. We find that using a simple regression model works as well or even better as designated methods when marker genes are used, while running much faster. The designated methods might show improved performance when using larger gene panels. Therefore, we suggest relying on a consensus of different methods to optimally integrate scRNA-seq data with SRT.

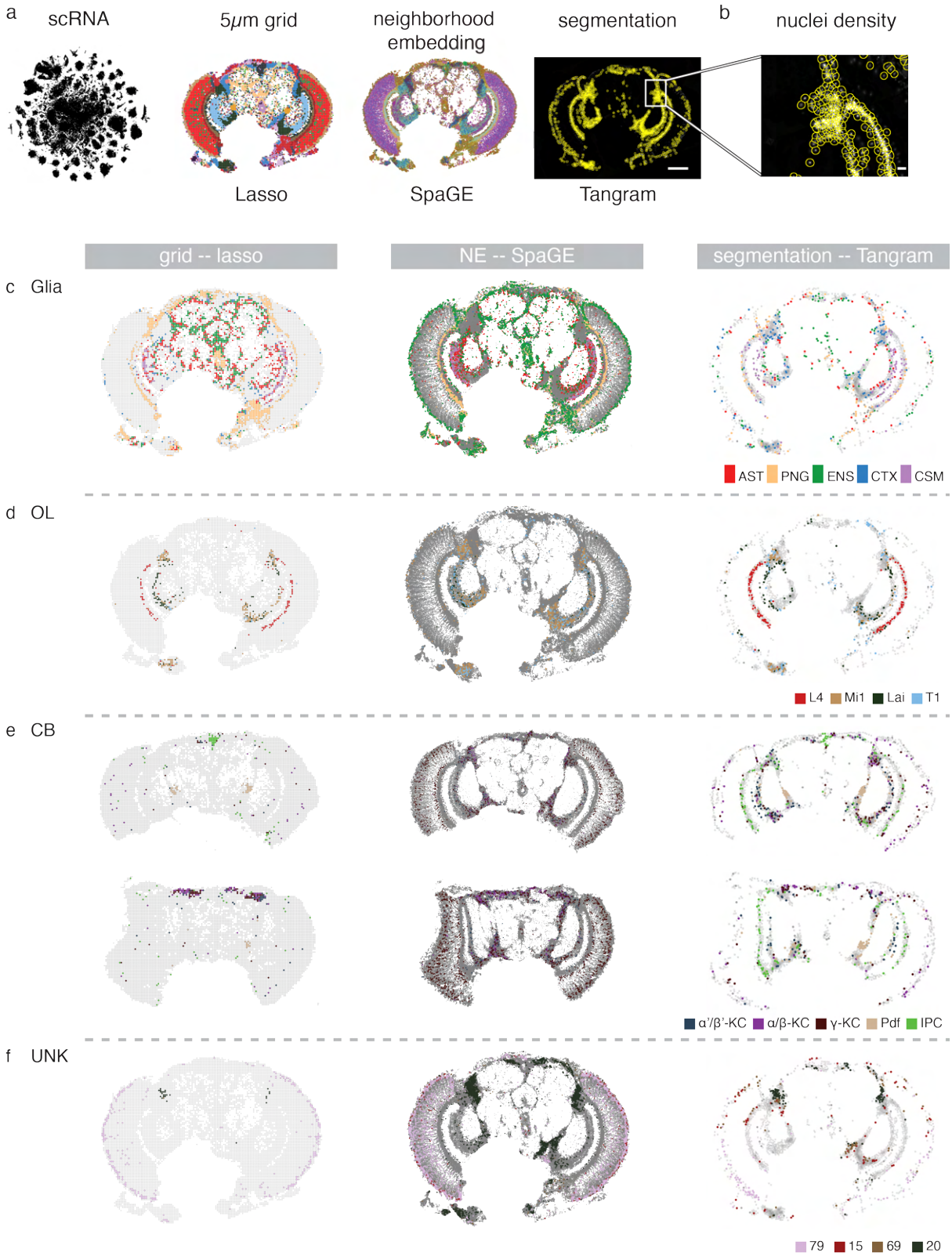

Figure 5. Comparison of different techniques for annotating the adult head samples. *a) Overview of different spatial analysis methods which were used to annotate SRT with labels from single-cell RNA-seq: grid-based, neighborhood embedding and nuclei segmentation. Scale bar represents 100 μm. b) Zoom-in on a high-density region with corresponding segmented nuclei. Scale bar represents 10 μm. c-f) Comparison of annotation of spatial data with single-cell RNA-seq for three different quantification methods. Grid-based*

squares/neighborhoods/nuclei are colored based on matching single-cell clusters for (c) glia, (d) optic lobe, (e) central brain and (f) unknown clusters. In (e) two brain slices are shown at different depths: central (top) and posterior (bottom). NE: neighborhood embedding.

Discussion

Here we present the first SRT dataset of the adult fly brain and body using highly multiplexed FISH. We used a 50-gene panel in the body, which made it possible to identify all major cell types in the adult male fly. Several measures of co-expression were used, which showed high concordance with published single-cell RNA-seq data (Li et al., 2022). Furthermore, expression of key marker genes could be used to identify the location of rare cell populations in the adult body. For example, expression of *Hml* showed the location of resident hemocytes, while *esg* was used to mark stem cells in the reproductive and intestinal tract. Therefore, SRT can be used to locate different cell populations in the fly body. Most of the published classical mRNA in situ hybridizations (Tomancak et al., 2002; Lécuyer et al., 2007; Jambor et al., 2015) as well as a recent high throughput FISH study used the easily accessible fly embryos (Wang et al., 2022), We expanded SRT here to the more complex anatomy of the adult fly, which requires sectioning and large data sampling, both at the microscope and at the computer. Thus, this proof of principle study will inspire future approaches that should be able increase gene throughput on the adult fly significantly. While SRT based on smFISH in mice (Yao et al., 2023) and humans (Fang et al., 2022) is limited to one tissue, large-scale brain atlases are being built and integrated with single-cell RNA-seq data. In flies, we show that both the brain and the whole-body can be sliced and imaged.

Compared to studies that focus on individual adult tissues, SRT of the entire adult fly made it possible to investigate the specificity of marker genes in the context of all tissues. We found that many markers are indeed highly specific to certain cell types, as we quantified for *Act88F* and *TpnC4* for the flight muscles. This also allowed us to estimate the false detection rate of the mRNA dots to less than 1%. Still, some marker genes showed additional unexpected expression (e.g., expression of *tin* and *TpnC4* in the ejaculatory bulb muscles), which was not detected in single-cell RNA-seq. Further, we found broad expression of LanB1 in many cell types, not only in hemocytes. As such, SRT can provide a more sensitive readout, including the spatial localization, and may inspire which other tissues might be interesting to investigate in the future when studying a particular gene function.

Performing SRT on the adult head led to additional challenges due to the small size of the head and the high density of the cell bodies in certain brain regions. Indeed, due to the small area of the head, samples often were tricky to adhere homogeneously to the slides and significant deformation occurred. An extra challenge occurs in the segmentation of nuclei, since *Drosophila* neuronal nuclei are multiple magnitudes smaller compared to human neuronal nuclei (5 cubic micrometers (Mu et al., 2021)). Here, expansion microscopy would help to increase the required resolution to reliably resolve each single nucleus (Fan et al., 2023; Steib et al., 2022). Expansion microscopy methods should be easily compatible with SRT (Fan et al., 2023; Pownall et al., 2023), which would be more challenging for single-molecule localization techniques that allow super-resolution imaging like DNA-PAINT, as they are harder but not impossible to multiplex (Agasti et al., 2017). Recent work on adult flight muscles showed that DNA-PAINT can indeed be applied to adult *Drosophila* tissue to achieve below 5 nm resolution (Schueder et al., 2023). Alternatively, 3D imaging could be used to improve nuclei segmentation (Pachitariu & Stringer, 2022).

In the head, we used a 100-gene panel and showed that this selection is sufficient to identify the major classes of cell types in the brain, including some very specific neuronal cell types like peptidergic neurons, Kenyon cells and different OL neurons. This provided a proof of principle of SRT in identifying cell types in the fly adult brain despite the small size of its cells and their high density.

SRT can serve as a bridge between different modalities, similar to the Rosetta stone, to link scRNA-seq atlases with spatial information, including connectomics in the brain. Using informative markers that were enriched in unknown clusters of single-cell RNA-seq data, we were able to locate the nuclei in the fly brain that showed expression of those markers. Hence, we were able to locate a series of formerly unknown cell clusters to defined brain regions. The next challenge lies in connecting these nuclei to the neuronal connectome using connectomics studies (Schlegel et al., 2023), in order to unambiguously identify the individual cell types. This nicely illustrates that SRT can provide the missing link between large scale single-cell transcriptomics studies and the morphology of complex neuronal architectures.

We explored several computational techniques to integrate SRT with single-cell RNA-seq including grid-rasterization, nuclei-segmentation and neighborhood embedding. Given the dense packing of the small nuclei in the fly brain, and the likely presence of mRNA transport away from the nucleus of origin, nuclei-segmentation leads to a loss of information compared to the other nuclei-unaware techniques. We further find that the mapping of some clusters is dominated by the presence of strong marker genes. Therefore, we predict strong improvements when it will be possible to use larger gene panels in the near future. Currently, sequencing-based methods such as Stereo-seq hold an advantage in number of genes that can be profiled (Wang et al., 2022), but smFISh-based approaches are scaling rapidly and will soon allow to routinely image 1000s of genes at higher resolutions (Fang et al., 2022).

The most exciting advantage of SRT compared to single-cell techniques applied to cells or nuclei in suspension, is the possibility to study mRNA localization within the tissue-context analyzed. As expected from findings in the embryo that reported a large number of mRNAs as non-homogeneously localized and thus likely transported (Jambor et al., 2015; Lécuyer et al., 2007; Tomancak et al., 2002), we found localized mRNAs in at least three different cell types. First, we found that different trypsin isoforms locate to opposite apical-basal locations in enterocytes of the adult gut. Such apical-basal mRNA transport processes are well described in the embryonic epidermis (Bullock et al., 2006), however, to our knowledge not yet known in the adult fly gut epidermis, where secretion of the enzymes at the correct side of the cell should be critical. Second, in the brain, we identified localized patterns of mRNAs coding for the neuropeptides *Pdf* and *Ilp2.* These mRNAs are likely transported into axons or dendrites, away from the cell body, a process often critical for brain development and function (Holt & Bullock, 2009). As both genes are very important regulators of adult physiology, the identified localization patterns may inspire future studies.

Third, in muscle cells, SRT revealed different patterns of mRNA distributions that suggest both mRNA transport and local synthesis in a subset of nuclei only. The latter is true for the terminal nuclei facing the muscle-tendon attachment sites that show increased localization and hence likely increased expression of the titin homolog *sls*. Sls protein is a critical component of the flight muscle sarcomere (Loreau et al., 2023) and also located at the terminal Z-disc linking the force-probing myofibrils to the tendon cells (Green et al., 2018). Interestingly, also in

mammalian muscles, it was recently found that the terminal muscle fiber nuclei that face the tendon cells apply a specialized transcriptional program (Kim et al., 2020; Esteves de Lima et al., 2021). Furthermore, we found here that within muscle fibers most mRNAs are non-randomly distributed with the most prominent patterns showing *sls* mRNA staying close to the nuclei that likely produce the RNA, whereas *Act88F* and *TpnC4* display alternating striped patterns that recapitulate the functional specializations within the muscle fibers, with locating myofibrils, mitochondria and ER to defined locations in muscle fiber (Luis & Schnorrer, 2021). It also has been proposed that ribosomes are concentrated at particular locations in mammalian muscles and build translational hotspots (Denes et al., 2021; Lewis et al., 2018; Rudolph et al., 2019). Whether such concentrations exist in fly muscles is not known. Hence, it will require future investigations to identify the functional significance of localizing mRNAs to particular localizations only and to identify the localization mechanisms.

To conclude, we have shown that medium throughput SRT on entire fly head and body samples is methodologically possible and leads to informative new discoveries that will spark interesting follow-up studies. All our data can be freely explored on https://spatialfly.aertslab.org. This has opened avenues for potential full 3D slicing and imaging of an adult fly in its entirety at high resolution in the near future.

Methods

Full fly sectioning

Before preparation, to ensure full adult development, adult male Luminy flies were isolated and left for 3 days at 25°C. After this step, the flies were put on ice for 15 minutes, and their wings were clipped. Flies were then transferred to a freezing mold, alive, embedded in optimal cutting temperature compound (OCT compound, VWR), and frozen in liquid nitrogen. Flies were sectioned with a cryostat (Leica CM 3050 S, Leica Biosystems, Germany). 10 µm sections were transferred to coverslips coated with gelatin (porcine skin, 300g Bloom Type A, Merck) and stored at -80℃.

Fly head sectioning

Adult flies (male and females) were anesthetized on a fly pad using CO_2 gas, to cut off their heads with a scalpel. Heads were then placed on a pre-cooled metal surface on dry ice and covered with a drop of OCT. Frozen OCT blocks were stored at -80℃ until sectioning. Sections of 10 µm thickness were produced with a Leica CM3050 S cryostat and placed on uncoated coverslips, which were stored at -80℃.

Molecular Cartography

a. Gene selection and probe design

Guided by the fly cell atlas, 150 genes were selected to be the most informative for spatial transcriptomics, 50 genes for the whole-body samples (Table S1) and 100 genes for the head samples (Table S2). These genes were selected based on different criteria including: marking specific cell populations, strong single-cell co-expression, marking unknown cell populations and showing broad expression.

The probes for the selected genes were designed using Resolve's proprietary design algorithm. To speed up the process, the calculation of computationally expensive parts, especially the off-target searches, the selection of probe sequences was not performed randomly, but limited to sequences with high success rates. To filter highly repetitive regions, the abundance of k-mers was obtained from the background transcriptome using Jellyfish (Marçais & Kingsford, 2011). Every target sequence was scanned once for all k-mers and those regions with rare k-mers were preferred as seeds for full probe design. A probe candidate was generated by extending a seed sequence until a certain target stability was reached. A set of simple rules was applied to discard sequences that were found experimentally to cause problems. After these fast screens, every kept probe candidate was mapped to the background transcriptome using ThermonucleotideBLAST (Gans & Wolinsky, 2008) and probes with stable off-target hits were discarded. Specific probes were then scored based on the number of on-target matches (isoforms), which were weighted by their associated APPRIS level (Rodriguez et al., 2018), favoring principal isoforms over others. A bonus was added if the binding site was inside the protein-coding region. From the pool of accepted probes, the final set was composed by greedily picking the highest scoring probes. Catalog numbers for the specific probes are available upon request at Resolve Biosciences.

b. Molecular Cartography

Samples were then sent to Resolve Biosciences on dry ice for analysis. Upon arrival, tissue sections were thawed and rehydrated with isopropanol, followed by 1-min washes in 95% ethanol and 70% ethanol at room temperature. The samples were used for Molecular Cartography (100-plex combinatorial single molecule fluorescence in situ hybridization) according to the manufacturer's instructions (protocol v.1.3; available for registered users), starting with the aspiration of ethanol and the addition of buffer DST1 followed by tissue priming and hybridization. Briefly, tissues were primed for 30 min at 37 °C followed by overnight hybridization of all probes specific for the target genes (see below for probe design details and target list). Samples were washed the next day to remove excess probes and fluorescently tagged in a two-step color development process. Regions of interest were imaged as described below and fluorescent signals were removed during decolorization. Color development, imaging and decolorization were repeated for multiple cycles to build a unique combinatorial code for every target gene that was derived from raw images as described below.

c. Imaging

Samples were imaged on a Zeiss Celldiscoverer 7, using the ×50 Plan Apochromat water immersion objective with an NA of 1.2 and the ×0.5 magnification changer, resulting in a ×25 final magnification. Standard CD7 LED excitation light source, filters and dichroic mirrors were used together with customized emission filters optimized for detecting specific signals. Excitation time per image was 1,000 ms for each channel (4,6-diamidino-2-phenylindole (DAPI) was 20 ms). A z-stack was taken at each region with a distance per z-slice according to the Nyquist–Shannon sampling theorem. The custom CD7 CMOS camera (Zeiss Axiocam Mono 712) was used. For each region, a z-stack per fluorescent color (two colors) was imaged per imaging round. A total of eight imaging rounds were conducted for each position, resulting in 16 z-stacks per region. The completely automated imaging process per round (including water immersion generation and precise relocation of regions to image in all three dimensions) was realized by a custom Python script using the scripting API of the Zeiss ZEN software (open application development).

d. Spot segmentation

The algorithms for spot segmentation were written in Java and are based on the ImageJ library functionalities. The iterative closest point algorithm is written in C++ based on the libpointmatcher library (https://github.com/ethz-asl/libpointmatcher).

e. Preprocessing

As a first step, all images were corrected for background fluorescence. A target value for the allowed number of maxima was determined based upon the area of the slice in μm² multiplied by the factor 0.5. This factor was empirically optimized. The brightest maxima per plane were determined, based upon an empirically optimized threshold. The number and location of the respective maxima was stored. This procedure was conducted for every image slice independently. Maxima that did not have a neighboring maximum in an adjacent slice (called a z group) were excluded. The resulting maxima list was further filtered in an iterative loop by adjusting the allowed thresholds for (Babs-Bback) and (Bperi-Bback) to reach a feature target value (Babs, absolute brightness; Bback, local background; and Bperi, background of periphery within one pixel). These feature target values were based upon the volume of the

three-dimensional (3D) image. Only maxima still in a z group of at least two after filtering were passing the filter step. Each z group was counted as one hit. The members of the z groups with the highest absolute brightness were used as features and written to a file. They resemble a 3D point cloud.

f. Final signal segmentation and decoding

To align the raw data images from different imaging rounds, images had to be corrected. To do so the extracted feature point clouds were used to find the transformation matrices. For this purpose, an iterative closest point cloud algorithm was used to minimize the error between two point clouds. The point clouds of each round were aligned to the point cloud of round one (reference point cloud). The corresponding point clouds were stored for downstream processes. Based upon the transformation matrices the corresponding images were processed by a rigid transformation using trilinear interpolation. The aligned images were used to create a profile for each pixel consisting of 16 values (16 images from two color channels in eight imaging rounds). The pixel profiles were filtered for variance from zero normalized by total brightness of all pixels in the profile. Matched pixel profiles with the highest score were assigned as an ID to the pixel. Pixels with neighbors having the same ID were grouped. The pixel groups were filtered by group size, number of direct adjacent pixels in group and number of dimensions with size of two pixels. The local 3D maxima of the groups were determined as potential final transcript locations. Maxima were filtered by number of maxima in the raw data images where a maximum was expected. Remaining maxima were further evaluated by the fit to the corresponding code. The remaining maxima were written to the results file and considered to resemble transcripts of the corresponding gene. The ratio of signals matching to codes used in the experiment and signals matching to codes not used in the experiment were used as estimation for specificity (false positives).

From Resolve Biosciences, the authors received the raw DAPI signal containing tiff image files, with gene localization count tables.

g. Gene visualization

Genes were plotted using Python scripts. Marker sizes were scaled by gene density to increase visibility of patterns.

Clustering analysis of mRNA species based on proximity

Based on the observation that groups of mRNA species appeared to cluster into separated regions of sections, we devised a simple method to automatically extract these regions based on the proximity of different mRNA. mRNA species that were identified as being close were then gathered into the same cluster.

In practice, we first computed the proximity of mRNA species by pair (see Fig. S5). Each localization of two mRNA species was transformed into disks of fixed diameters, each disk being centered on a given mRNA localization; the diameter used here was 4 µm. To generate one surface for a species and avoid counting multiple times the same area, disks of a given mRNA species were merged if they were overlapping. We then computed their overlap surface from the surfaces obtained from two different mRNA species. The proximity of one mRNA

species (mRNA1) versus the over one (mRNA2) was defined as the ratio between the overlap surface and surface of the second mRNA species (mRNA2):

$$Proximity\ mRNA_{1\ in\ 2} = \frac{Overlap\ mRNA_{1\ and\ 2}}{Surface\ mRNA_2}$$

Reciprocally,

$$Proximity\ mRNA_{2\ in\ 1} = \frac{Overlap\ mRNA_{1\ and\ 2}}{Surface\ mRNA_1}$$

The calculation of proximity then allowed us to define a distance between two mRNA species:

$$Distance\ mRNA_{1\ and\ 2} = 2 - (Proximity\ mRNA_{1\ in\ 2} + Proximity\ mRNA_{2\ in\ 1})$$

mRNA species that show perfect overlap get a distance of 0 in this metric, whereas mRNA species that do not show any overlap would get a distance of 2.

Finally, this metric was used in a hierarchical clustering analysis using Ward's method. Clusters were then extracted from this analysis.

5x5 µm grid analysis

a. Quantification

Samples were rasterized in a square grid of 36 by 36 pixels (1 pixel = 0.138 µm, 36 pixels = 4.968 µm). All counts within this area were summed up. This led to a square by gene matrix, with for every square the mean x and y spatial coordinates of the square's dimensions.

b. SCANPY body

All body samples (5) were analyzed together in SCANPY (1.9.3) (Wolf et al., 2018). An increment of 1000 was added to both spatial x- and y-coordinates to arrange all samples together. Only squares with more than 3 counts were kept, leading to 132,642 squares with information for 50 genes. The data was subsequently normalized with 10,000 as size factor and log transformed. This matrix was then used as input for PCA, after which 40 components were retained by evaluating variance ratio plots. Harmony was then used to correct for batch effects between samples. 30 PCs were used to calculate neighbors, Leiden clustering (resolutions 0.2, 0.5, 1 and 2) and UMAP embeddings.

c. SCANPY head

All head samples (13) were analyzed together in SCANPY (1.9.3) (Wolf et al., 2018). An increment of 1000 was added to both spatial x- and y-coordinates to arrange all samples together. Only squares with more than 3 counts were kept, leading to 83,064 squares with information for 99 genes (*ninaE* was discarded from most samples due to optical crowding). The data was subsequently normalized with 10,000 as size factor and log transformed. This matrix was then used as input for PCA, after which 30 components were retained by evaluating variance ratio plots. Harmony was then used to correct for batch effects between samples. 25 PCs were used to calculate neighbors, Leiden clustering (resolutions 0.2, 0.5, 1 and 2) and UMAP embeddings.

d. Head OL vs CB vs PR differential expression

Leiden resolution 1 was used to create average gene expression profiles for clusters. Clusters with mean expression of para>0.05 were selected as neuronal clusters. These were subsequently manually assigned to either Photoreceptor (PR), Optic lobe (OL) or Central brain (CB) regions based on location. Next, the rank_genes_groups function from SCANPY was used to calculate differential genes for the regions based on a t-test.

e. Gene set enrichment

In the body, we selected marker genes that were assigned to several categories. We then summed the expression of genes belonging to the same category to derive gene set signatures. The following gene sets were used: muscle (*Mhc*, *sls*, *CG32121*), neurons (*elav*, *Syt1*, *Sh*, *acj6*, *ey*, *VAChT*, *Gad1*, *VGlut*, *nAChRalpha7*), glia (*repo*, *alrm*), epithelia (pure: *grh*, *hth*, gut: *alphaTry*, *betaTry*), heart (*tin*, *Hand*), fat body (*AkhR*, *FASN2*), oenocyte (*FASN2*), male reproductive system (*Awh*, *eyg*, *svp*) and hemocytes (*Hml*). Spots in the grid were assigned to a category based on Z-scores. If z-normalised expression>1, the spot was assigned to the category. When conflicts arose, the following hierarchy was used: muscle > epithelia > glia > neurons > male reproductive system > fat body > oenocyte > hemocyte > heart.

f. Lasso matching

We used lasso regression as implemented in sklearn (1.2.2). Averaged gene expression profiles of single-cell clusters were matched with expression profiles of the grid-based squares. The regression model was run using Lasso(alpha=1, positive=True), forcing all coefficients to be positive, with all genes. Higher weights for the single-cell clusters corresponds to a higher similarity between the cluster and the square. We only used weights > 0.2 as confident matches. Spots were then assigned to the cluster based on the highest weight.

Nuclei segmentation

Nuclei in DAPI images were segmented with Cellprofiler (version 4.0.7) (Stirling et al., 2021). Features of the DAPI images were enhanced (*EnhanceOrSuppressFeatures, Enhance, Speckles*) using a feature size of 100 pixels. Initial nuclei were detected using a size of 10-100 pixels, global Otsu thresholding with two classes, intensity for distinguishing clumped objects, *propagate* for drawing dividing lines. Initial nuclei were extended by 25 pixels. We then collected all transcripts inside a segmented cell to compute counts of each gene per segmented cell.

Tangram

Tangram (version 1.0.2) (Biancalani et al., 2021) was used to project cell type labels from single cell data. Here we used the *cell* mapping mode to map single cell data to each spatial slice separately. The mapping was computed on a NVIDIA A100-SXM4-80GB GPU. Prior to computing the mapping, segmented cells with less than three expressed genes and genes that were expressed in less than three cells were removed. Single cells and segmented cells were log-normalized in SCANPY (Wolf et al., 2018) with a target-sum of 10^4. All genes that

are shared between the spatial data and single cell data after filtering were used for the mapping. Cell type labels for fly head samples were assigned separately for Glia, optic lobe (OL), central brain (CB) and unknown clusters (UNK) by considering only the subset cell types that we grouped into the category. A cell type label was assigned to a segmented cell based on the 95%-quantile of the mapping scores for a cell type (unless stated otherwise) if this resulted in a unique label assignment. Cell type labels for the grid rasterized spatial data were assigned in the same manner as we did for the segmented cells. The only exception being, that we downsampled the number of cells to a maximum of 5000 cells per cell type in the single cell data to limit the amounts of required video memory.

Neighborhood embedding and SpaGE

Segmentation-free analysis of fly head and body SRT datasets have been carried out using spage2vec (Partel & Wählby, 2021). Briefly, spatial graphs of all mRNAs are first constructed for each different sample. Then, a graph convolution neural network trained in a self-superwise fashion projects each mRNA into an embedding space based on its spatial neighborhood composition. Such that mRNAs that share similar neighbors are mapped close together in the embedding space. Downstream clustering or visualization of mRNA embeddings unveil spatial gene expression patterns described by specific combinations of genes at subcellular resolution. Pseudo-cell counts have been generated for each mRNA by aggregating counts of *k* neighboring mRNAs (i.e. k=100) in the embedding space. Finally, integration of reference scRNA-seq datasets with spatial pseudo-cell counts have been implemented by projecting both datasets into a common shared space using SpaGE (Abdelaal et al., 2020). Thereafter, cell type labels have been transferred from scRNA-seq cells to spatial pseudo-cells by kNN imputation (with k=100).

mRNA localization in muscle - distance to nuclei

For every detected mRNA molecule, the distance to the closest nucleus was calculated. First, we calculated a mask to segment the indirect flight muscle using *Act88F* mRNA spots. Using opencv2, we performed a Gaussian blur (ksize=5x5, sigma=1), followed by two erosion steps (5x5 and 4x4) to remove sparse signals. Then the spots were dilated thrice (50x50), followed by a final Gaussian blur (ksize=5x5, sigma=1). Only other mRNA species that overlap with this mask were kept for the distance analysis.

The nucleus segmentation was loaded as a black-white image. The nonzero function from opencv2 was used to find segmented pixels. Then for each mRNA spot, Euclidean distances were calculated to the segmented pixels, after which they were assigned to the closest pixel. To optimize the calculations, joblib's Parallel function was used. This was repeated over all body samples and results were combined. Only genes for which at least 100 mRNA spots were detected across samples and not localized at the edges (faulty segmentation along the muscle boundary) were kept: *Act88F*, *Mhc*, *TpnC4*, *sls*, *salm* and *CG32121*.

Acknowledgements

We thank VIB Tech Watch, Resolve Biosciences, and Jeroen Aerts for facilitating early access to the Molecular Cartography platform. Computing was performed on VSC (Vlaams Supercomputer Centrum).

Funding

This work was in part funded by ERC AdG Genome2Cells (S.A.; 101054387); a FWO PhD Fellowship to (J.J.; 1199518N); a FWO Postdoctoral fellowship (N.H.; 1273822N); GP was funded by Opening The Future. This work was supported by the Centre National de la Recherche Scientifique (CNRS, F.S.), Aix-Marseille University (P.M.), the European Research Council under the European Union's Horizon 2020 Programme (ERC-2019-SyG 856118 F.S.), FP/2007-2013)/ERC Grant 310939 (F.S.) and by funding from France 2030, the French Government program managed by the French National Research Agency (ANR-16-CONV-0001) and from Excellence Initiative of Aix-Marseille University - A*MIDEX (Turing Centre for Living Systems).

Data Availability

All data (raw DAPI .tiff files, mRNA localization tables) are available on https://spatialfly.aertslab.org/. Supplementary Table S1 and S2 list the genes used as probes. Probe design was performed by Resolve Biosciences. Gene panels are commercially available for use.

Code Availability

Code for the website (https://spatialfly.aertslab.org/) is available on Github (https://github.com/aertslab/spatial_fly_website). In this folder scripts to perform grid, segmentation and neighborhood-embedding analysis can also be found. A pipeline can be found here: https://github.com/aertslab/SpatialNF.

Contributions

S.A., F.S. and J.J. conceived the study. K.S. and J.I. prepared head samples. P.M. prepared body samples. J.J., P.M., N.H. and G.P. performed computational analyses. J.J. performed grid-based rasterization. P.M. performed mRNA overlap analysis. N.H. performed nuclei segmentation and Tangram label transfer. G.P. performed neighborhood embedding analysis. F.S., P.M. and J.J. performed muscle analysis. J.J. created the website with assistance of G.H. N.H. and G.P. developed the spatial analysis pipeline. J.J., F.S., S.A. and P.M. wrote the manuscript.

References

Abdelaal, T., Mourragui, S., Mahfouz, A., & Reinders, M. J. T. (2020). SpaGE: Spatial Gene Enhancement using scRNA-seq. *Nucleic Acids Research*, *48*(18), e107. https://doi.org/10.1093/nar/gkaa740

Agasti, S. S., Wang, Y., Schueder, F., Sukumar, A., Jungmann, R., & Yin, P. (2017). DNA-barcoded labeling probes for highly multiplexed Exchange-PAINT imaging. *Chemical Science*, *8*(4), 3080–3091. https://doi.org/10.1039/C6SC05420J

Agianian, B., Krzic, U., Qiu, F., Linke, W. A., Leonard, K., & Bullard, B. (2004). A troponin switch that regulates muscle contraction by stretch instead of calcium. *The EMBO Journal*, *23*(4), 772–779. https://doi.org/10.1038/sj.emboj.7600097

Avellaneda, J., Rodier, C., Daian, F., Brouilly, N., Rival, T., Luis, N. M., & Schnorrer, F. (2021). Myofibril and mitochondria morphogenesis are coordinated by a mechanical feedback mechanism in muscle. *Nature Communications*, *12*(1), Article 1. https://doi.org/10.1038/s41467-021-22058-7

Benton, R. (2022). Drosophila olfaction: Past, present and future. *Proceedings of the Royal Society B: Biological Sciences*, *289*(1989), 20222054. https://doi.org/10.1098/rspb.2022.2054

Biancalani, T., Scalia, G., Buffoni, L., Avasthi, R., Lu, Z., Sanger, A., Tokcan, N., Vanderburg, C. R., Segerstolpe, Å., Zhang, M., Avraham-Davidi, I., Vickovic, S., Nitzan, M., Ma, S., Subramanian, A., Lipinski, M., Buenrostro, J., Brown, N. B., Fanelli, D., … Regev, A. (2021). Deep learning and alignment of spatially resolved single-cell transcriptomes with Tangram. *Nature Methods*, *18*(11), Article 11. https://doi.org/10.1038/s41592-021-01264-7

Bruusgaard, J. C., Liestøl, K., Ekmark, M., Kollstad, K., & Gundersen, K. (2003). Number and spatial distribution of nuclei in the muscle fibres of normal mice studied in vivo. *The Journal of Physiology*, *551*(Pt 2), 467–478. https://doi.org/10.1113/jphysiol.2003.045328

Bullock, S. L., Nicol, A., Gross, S. P., & Zicha, D. (2006). Guidance of bidirectional motor complexes by mRNA cargoes through control of dynein number and activity. *Current Biology: CB*, *16*(14), 1447–1452. https://doi.org/10.1016/j.cub.2006.05.055

Chaturvedi, D., Reichert, H., Gunage, R. D., & VijayRaghavan, K. (2017). Identification and functional characterization of muscle satellite cells in Drosophila. *eLife*, *6*, e30107. https://doi.org/10.7554/eLife.30107

Chen, K. H., Boettiger, A. N., Moffitt, J. R., Wang, S., & Zhuang, X. (2015). Spatially resolved, highly multiplexed RNA profiling in single cells. *Science*, *348*(6233), aaa6090. https://doi.org/10.1126/science.aaa6090

Davie, K., Janssens, J., Koldere, D., De Waegeneer, M., Pech, U., Kreft, Ł., Aibar, S., Makhzami, S., Christiaens, V., Bravo González-Blas, C., Poovathingal, S., Hulselmans, G., Spanier, K. I., Moerman, T., Vanspauwen, B., Geurs, S., Voet, T., Lammertyn, J., Thienpont, B., … Aerts, S. (2018). A Single-Cell Transcriptome Atlas of the Aging Drosophila Brain. *Cell*, *174*(4), 982-998.e20. https://doi.org/10.1016/j.cell.2018.05.057

Denes, L. T., Kelley, C. P., & Wang, E. T. (2021). Microtubule-based transport is essential to distribute RNA and nascent protein in skeletal muscle. *Nature Communications*, *12*(1), Article 1. https://doi.org/10.1038/s41467-021-26383-9

Díaz, M. M., Schlichting, M., Abruzzi, K. C., Long, X., & Rosbash, M. (2019). Allatostatin-C/AstC-R2 Is a Novel Pathway to Modulate the Circadian Activity Pattern in Drosophila. *Current Biology*, *29*(1), 13-22.e3. https://doi.org/10.1016/j.cub.2018.11.005

Eng, C.-H. L., Lawson, M., Zhu, Q., Dries, R., Koulena, N., Takei, Y., Yun, J., Cronin, C., Karp, C., Yuan, G.-C., & Cai, L. (2019). Transcriptome-scale super-resolved imaging in tissues by RNA seqFISH+. *Nature*, *568*(7751), Article 7751. https://doi.org/10.1038/s41586-019-1049-y

Esteves de Lima, J., Blavet, C., Bonnin, M.-A., Hirsinger, E., Comai, G., Yvernogeau, L., Delfini, M.-C., Bellenger, L., Mella, S., Nassari, S., Robin, C., Schweitzer, R.,

Fournier-Thibault, C., Jaffredo, T., Tajbakhsh, S., Relaix, F., & Duprez, D. (2021). Unexpected contribution of fibroblasts to muscle lineage as a mechanism for limb muscle patterning. *Nature Communications*, *12*(1), Article 1. https://doi.org/10.1038/s41467-021-24157-x

Fan, Y., Andrusivová, Ž., Wu, Y., Chai, C., Larsson, L., He, M., Luo, L., Lundeberg, J., & Wang, B. (2023). Expansion spatial transcriptomics. *Nature Methods*, *20*(8), Article 8. https://doi.org/10.1038/s41592-023-01911-1

Fang, R., Xia, C., Close, J. L., Zhang, M., He, J., Huang, Z., Halpern, A. R., Long, B., Miller, J. A., Lein, E. S., & Zhuang, X. (2022). Conservation and divergence of cortical cell organization in human and mouse revealed by MERFISH. *Science*, *377*(6601), 56–62. https://doi.org/10.1126/science.abm1741

Folker, E., & Baylies, M. (2013). Nuclear positioning in muscle development and disease. *Frontiers in Physiology*, *4*. https://www.frontiersin.org/articles/10.3389/fphys.2013.00363

Fyrberg, E. A., Mahaffey, J. W., Bond, B. J., & Davidson, N. (1983). Transcripts of the six Drosophila actin genes accumulate in a stage- and tissue-specific manner. *Cell*, *33*(1), 115–123. https://doi.org/10.1016/0092-8674(83)90340-9

Gans, J. D., & Wolinsky, M. (2008). Improved assay-dependent searching of nucleic acid sequence databases. *Nucleic Acids Research*, *36*(12), e74. https://doi.org/10.1093/nar/gkn301

Green, H. J., Griffiths, A. G., Ylänne, J., & Brown, N. H. (2018). Novel functions for integrin-associated proteins revealed by analysis of myofibril attachment in Drosophila. *eLife*, *7*, e35783. https://doi.org/10.7554/eLife.35783

Grenier, T., & Leulier, F. (2020). How commensal microbes shape the physiology of Drosophila melanogaster. *Current Opinion in Insect Science*, *41*, 92–99. https://doi.org/10.1016/j.cois.2020.08.002

Han, X., Wang, M., Liu, C., Trush, O., Takayama, R., Akiyama, T., Naito, T., Tomomizu, T., Imamura, K., & Sato, M. (2020). DWnt4 and DWnt10 Regulate Morphogenesis and

Arrangement of Columnar Units via Fz2/PCP Signaling in the Drosophila Brain. *Cell Reports*, *33*(4), 108305. https://doi.org/10.1016/j.celrep.2020.108305

Holt, C. E., & Bullock, S. L. (2009). Subcellular mRNA Localization in Animal Cells and Why It Matters. *Science*, *326*(5957), 1212–1216. https://doi.org/10.1126/science.1176488

Jambor, H., Surendranath, V., Kalinka, A. T., Mejstrik, P., Saalfeld, S., & Tomancak, P. (2015). Systematic imaging reveals features and changing localization of mRNAs in Drosophila development. *eLife*, *4*, e05003. https://doi.org/10.7554/eLife.05003

Jiang, H., & Edgar, B. A. (2011). Intestinal stem cells in the adult Drosophila midgut. *Experimental Cell Research*, *317*(19), 2780–2788. https://doi.org/10.1016/j.yexcr.2011.07.020

Kaya-Çopur, A., Marchiano, F., Hein, M. Y., Alpern, D., Russeil, J., Luis, N. M., Mann, M., Deplancke, B., Habermann, B. H., & Schnorrer, F. (2021). The Hippo pathway controls myofibril assembly and muscle fiber growth by regulating sarcomeric gene expression. *eLife*, *10*, e63726. https://doi.org/10.7554/eLife.63726

Kim, M., Franke, V., Brandt, B., Lowenstein, E. D., Schöwel, V., Spuler, S., Akalin, A., & Birchmeier, C. (2020). Single-nucleus transcriptomics reveals functional compartmentalization in syncytial skeletal muscle cells. *Nature Communications*, *11*(1), Article 1. https://doi.org/10.1038/s41467-020-20064-9

Klein, A. M., Mazutis, L., Akartuna, I., Tallapragada, N., Veres, A., Li, V., Peshkin, L., Weitz, D. A., & Kirschner, M. W. (2015). Droplet Barcoding for Single-Cell Transcriptomics Applied to Embryonic Stem Cells. *Cell*, *161*(5), 1187–1201. https://doi.org/10.1016/j.cell.2015.04.044

Lécuyer, E., Yoshida, H., Parthasarathy, N., Alm, C., Babak, T., Cerovina, T., Hughes, T. R., Tomancak, P., & Krause, H. M. (2007). Global Analysis of mRNA Localization Reveals a Prominent Role in Organizing Cellular Architecture and Function. *Cell*, *131*(1), 174–187. https://doi.org/10.1016/j.cell.2007.08.003

Lewis, Y. E., Moskovitz, A., Mutlak, M., Heineke, J., Caspi, L. H., & Kehat, I. (2018). Localization of transcripts, translation, and degradation for spatiotemporal sarcomere

maintenance. *Journal of Molecular and Cellular Cardiology*, *116*, 16–28. https://doi.org/10.1016/j.yjmcc.2018.01.012

Li, H., Janssens, J., De Waegeneer, M., Kolluru, S. S., Davie, K., Gardeux, V., Saelens, W., David, F. P. A., Brbić, M., Spanier, K., Leskovec, J., McLaughlin, C. N., Xie, Q., Jones, R. C., Brueckner, K., Shim, J., Tattikota, S. G., Schnorrer, F., Rust, K., … Zinzen, R. P. (2022). Fly Cell Atlas: A single-nucleus transcriptomic atlas of the adult fruit fly. *Science*, *375*(6584), eabk2432. https://doi.org/10.1126/science.abk2432

Loreau, V., Rees, R., Chan, E. H., Taxer, W., Gregor, K., Mußil, B., Pitaval, C., Luis, N. M., Mangeol, P., Schnorrer, F., & Görlich, D. (2023). A nanobody toolbox to investigate localisation and dynamics of Drosophila titins and other key sarcomeric proteins. *eLife*, *12*, e79343. https://doi.org/10.7554/eLife.79343

Lu, T.-C., Brbić, M., Park, Y.-J., Jackson, T., Chen, J., Kolluru, S. S., Qi, Y., Katheder, N. S., Cai, X. T., Lee, S., Chen, Y.-C., Auld, N., Liang, C.-Y., Ding, S. H., Welsch, D., D'Souza, S., Pisco, A. O., Jones, R. C., Leskovec, J., … Li, H. (2023). Aging Fly Cell Atlas identifies exhaustive aging features at cellular resolution. *Science*, *380*(6650), eadg0934. https://doi.org/10.1126/science.adg0934

Lubeck, E., Coskun, A. F., Zhiyentayev, T., Ahmad, M., & Cai, L. (2014). Single-cell in situ RNA profiling by sequential hybridization. *Nature Methods*, *11*(4), Article 4. https://doi.org/10.1038/nmeth.2892

Luis, N. M., & Schnorrer, F. (2021). Mechanobiology of muscle and myofibril morphogenesis. *Cells & Development*, *168*, 203760. https://doi.org/10.1016/j.cdev.2021.203760

Marçais, G., & Kingsford, C. (2011). A fast, lock-free approach for efficient parallel counting of occurrences of k-mers. *Bioinformatics*, *27*(6), 764–770. https://doi.org/10.1093/bioinformatics/btr011

Martin, K. C., & Ephrussi, A. (2009). mRNA Localization: Gene Expression in the Spatial Dimension. *Cell*, *136*(4), 719–730. https://doi.org/10.1016/j.cell.2009.01.044

Matsubayashi, Y., Louani, A., Dragu, A., Sánchez-Sánchez, B. J., Serna-Morales, E., Yolland, L., Gyoergy, A., Vizcay, G., Fleck, R. A., Heddleston, J. M., Chew, T.-L.,

Siekhaus, D. E., & Stramer, B. M. (2017). A Moving Source of Matrix Components Is Essential for De Novo Basement Membrane Formation. *Current Biology: CB*, *27*(22), 3526-3534.e4. https://doi.org/10.1016/j.cub.2017.10.001

McNeill, H., Yang, C. H., Brodsky, M., Ungos, J., & Simon, M. A. (1997). Mirror encodes a novel PBX-class homeoprotein that functions in the definition of the dorsal-ventral border in the Drosophila eye. *Genes & Development*, *11*(8), 1073–1082. https://doi.org/10.1101/gad.11.8.1073

Moses, L., & Pachter, L. (2022). Museum of spatial transcriptomics. *Nature Methods*, *19*(5), 534–546. https://doi.org/10.1038/s41592-022-01409-2

Mu, S., Yu, S., Turner, N. L., McKellar, C. E., Dorkenwald, S., Collman, F., Koolman, S., Moore, M., Morejohn, S., Silverman, B., Willie, K., Willie, R., Bland, D., Burke, A., Ashwood, Z., Luther, K., Castro, M., Ogedengbe, O., Silversmith, W., … Seung, H. S. (2021). *3D reconstruction of cell nuclei in a full Drosophila brain* (p. 2021.11.04.467197). bioRxiv. https://doi.org/10.1101/2021.11.04.467197

Özel, M. N., Simon, F., Jafari, S., Holguera, I., Chen, Y.-C., Benhra, N., El-Danaf, R. N., Kapuralin, K., Malin, J. A., Konstantinides, N., & Desplan, C. (2021). Neuronal diversity and convergence in a visual system developmental atlas. *Nature*, *589*(7840), 88–95. https://doi.org/10.1038/s41586-020-2879-3

Pachitariu, M., & Stringer, C. (2022). Cellpose 2.0: How to train your own model. *Nature Methods*, *19*(12), Article 12. https://doi.org/10.1038/s41592-022-01663-4

Partel, G., & Wählby, C. (2021). Spage2vec: Unsupervised representation of localized spatial gene expression signatures. *The FEBS Journal*, *288*(6), 1859–1870. https://doi.org/10.1111/febs.15572

Pech, U., Janssens, J., Schoovaerts, N., Makhzami, S., Hulselmans, G., Poovathingal, S., Aristoy, C. C., Bademosi, A. T., Swerts, J., Geens, A., Vilain, S., Aerts, S., & Verstreken, P. (2023). *Rescuing early Parkinson-induced hyposmia prevents dopaminergic system failure* (p. 2023.03.11.532176). bioRxiv. https://doi.org/10.1101/2023.03.11.532176

Pinheiro, H., Pimentel, M. R., Sequeira, C., Oliveira, L. M., Pezzarossa, A., Roman, W., & Gomes, E. R. (2021). mRNA distribution in skeletal muscle is associated with mRNA size. *Journal of Cell Science*, *134*(14), jcs256388. https://doi.org/10.1242/jcs.256388

Pownall, M. E., Miao, L., Vejnar, C. E., M'Saad, O., Sherrard, A., Frederick, M. A., Benitez, M. D. J., Boswell, C. W., Zaret, K. S., Bewersdorf, J., & Giraldez, A. J. (2023). Chromatin expansion microscopy reveals nanoscale organization of transcription and chromatin. *Science*, *381*(6653), 92–100. https://doi.org/10.1126/science.ade5308

Rodriguez, J. M., Rodriguez-Rivas, J., Di Domenico, T., Vázquez, J., Valencia, A., & Tress, M. L. (2018). APPRIS 2017: Principal isoforms for multiple gene sets. *Nucleic Acids Research*, *46*(D1), D213–D217. https://doi.org/10.1093/nar/gkx997

Rodriques, S. G., Stickels, R. R., Goeva, A., Martin, C. A., Murray, E., Vanderburg, C. R., Welch, J., Chen, L. M., Chen, F., & Macosko, E. Z. (2019). Slide-seq: A scalable technology for measuring genome-wide expression at high spatial resolution. *Science*, *363*(6434), 1463–1467. https://doi.org/10.1126/science.aaw1219

Rudolph, F., Hüttemeister, J., da Silva Lopes, K., Jüttner, R., Yu, L., Bergmann, N., Friedrich, D., Preibisch, S., Wagner, E., Lehnart, S. E., Gregorio, C. C., & Gotthardt, M. (2019). Resolving titin's lifecycle and the spatial organization of protein turnover in mouse cardiomyocytes. *Proceedings of the National Academy of Sciences*, *116*(50), 25126–25136. https://doi.org/10.1073/pnas.1904385116

Sarov, M., Barz, C., Jambor, H., Hein, M. Y., Schmied, C., Suchold, D., Stender, B., Janosch, S., Kj, V. V., Krishnan, R., Krishnamoorthy, A., Ferreira, I. R., Ejsmont, R. K., Finkl, K., Hasse, S., Kämpfer, P., Plewka, N., Vinis, E., Schloissnig, S., … Schnorrer, F. (2016). A genome-wide resource for the analysis of protein localisation in Drosophila. *eLife*, *5*, e12068. https://doi.org/10.7554/eLife.12068

Schaum, N., Karkanias, J., Neff, N. F., May, A. P., Quake, S. R., Wyss-Coray, T., Darmanis, S., Batson, J., Botvinnik, O., Chen, M. B., Chen, S., Green, F., Jones, R. C., Maynard, A., Penland, L., Pisco, A. O., Sit, R. V., Stanley, G. M., Webber, J. T., … Principal investigators. (2018). Single-cell transcriptomics of 20 mouse organs

creates a Tabula Muris. *Nature*, *562*(7727), Article 7727. https://doi.org/10.1038/s41586-018-0590-4

Schlegel, P., Yin, Y., Bates, A. S., Dorkenwald, S., Eichler, K., Brooks, P., Han, D. S., Gkantia, M., Santos, M. dos, Munnelly, E. J., Badalamente, G., Capdevila, L. S., Sane, V. A., Pleijzier, M. W., Tamimi, I. F. M., Dunne, C. R., Salgarella, I., Javier, A., Fang, S., … Jefferis, G. S. X. E. (2023). *Whole-brain annotation and multi-connectome cell typing quantifies circuit stereotypy in Drosophila* (p. 2023.06.27.546055). bioRxiv. https://doi.org/10.1101/2023.06.27.546055

Schönbauer, C., Distler, J., Jährling, N., Radolf, M., Dodt, H.-U., Frasch, M., & Schnorrer, F. (2011). Spalt mediates an evolutionarily conserved switch to fibrillar muscle fate in insects. *Nature*, *479*(7373), Article 7373. https://doi.org/10.1038/nature10559

Schueder, F., Mangeol, P., Chan, E. H., Rees, R., Schünemann, J., Jungmann, R., Görlich, D., & Schnorrer, F. (2023). Nanobodies combined with DNA-PAINT super-resolution reveal a staggered titin nanoarchitecture in flight muscles. *eLife*, *12*, e79344. https://doi.org/10.7554/eLife.79344

Sênos Demarco, R., Stack, B. J., Tang, A. M., Voog, J., Sandall, S. L., Southall, T. D., Brand, A. H., & Jones, D. L. (2022). Escargot controls somatic stem cell maintenance through the attenuation of the insulin receptor pathway in Drosophila. *Cell Reports*, *39*(3), 110679. https://doi.org/10.1016/j.celrep.2022.110679

Sokolowski, M. B. (2001). Drosophila: Genetics meets behaviour. *Nature Reviews Genetics*, *2*(11), Article 11. https://doi.org/10.1038/35098592

Solorzano, L., Partel, G., & Wählby, C. (2020). TissUUmaps: Interactive visualization of large-scale spatial gene expression and tissue morphology data. *Bioinformatics*, *36*(15), 4363–4365. https://doi.org/10.1093/bioinformatics/btaa541

Spletter, M. L., Barz, C., Yeroslaviz, A., Zhang, X., Lemke, S. B., Bonnard, A., Brunner, E., Cardone, G., Basler, K., Habermann, B. H., & Schnorrer, F. (2018). A transcriptomics resource reveals a transcriptional transition during ordered sarcomere morphogenesis in flight muscle. *eLife*, *7*, e34058. https://doi.org/10.7554/eLife.34058

Stahl, A. L., Charlton-Perkins, M., Buschbeck, E. K., & Cook, T. A. (2017). The cuticular nature of corneal lenses in Drosophila melanogaster. *Development Genes and Evolution*, *227*(4), 271–278. https://doi.org/10.1007/s00427-017-0582-7

Steib, E., Tetley, R., Laine, R. F., Norris, D. P., Mao, Y., & Vermot, J. (2022). TissUExM enables quantitative ultrastructural analysis in whole vertebrate embryos by expansion microscopy. *Cell Reports Methods*, *2*(10), 100311. https://doi.org/10.1016/j.crmeth.2022.100311

Stirling, D. R., Swain-Bowden, M. J., Lucas, A. M., Carpenter, A. E., Cimini, B. A., & Goodman, A. (2021). CellProfiler 4: Improvements in speed, utility and usability. *BMC Bioinformatics*, *22*(1), 433. https://doi.org/10.1186/s12859-021-04344-9

The Tabula Sapiens consortium. (2022). The Tabula Sapiens: A multiple-organ, single-cell transcriptomic atlas of humans. *Science*, *376*(6594), eabl4896. https://doi.org/10.1126/science.abl4896

Tomancak, P., Beaton, A., Weiszmann, R., Kwan, E., Shu, S., Lewis, S. E., Richards, S., Ashburner, M., Hartenstein, V., Celniker, S. E., & Rubin, G. M. (2002). Systematic determination of patterns of gene expression during Drosophila embryogenesis. *Genome Biology*, *3*(12), research0088.1. https://doi.org/10.1186/gb-2002-3-12-research0088

Wang, M., Hu, Q., Lv, T., Wang, Y., Lan, Q., Xiang, R., Tu, Z., Wei, Y., Han, K., Shi, C., Guo, J., Liu, C., Yang, T., Du, W., An, Y., Cheng, M., Xu, J., Lu, H., Li, W., … Liu, L. (2022). High-resolution 3D spatiotemporal transcriptomic maps of developing Drosophila embryos and larvae. *Developmental Cell*, *57*(10), 1271-1283.e4. https://doi.org/10.1016/j.devcel.2022.04.006

Wolf, F. A., Angerer, P., & Theis, F. J. (2018). SCANPY: Large-scale single-cell gene expression data analysis. *Genome Biology*, *19*(1), 15. https://doi.org/10.1186/s13059-017-1382-0

Yao, Z., Velthoven, C. T. J. van, Kunst, M., Zhang, M., McMillen, D., Lee, C., Jung, W., Goldy, J., Abdelhak, A., Baker, P., Barkan, E., Bertagnolli, D., Campos, J., Carey, D.,

Casper, T., Chakka, A. B., Chakrabarty, R., Chavan, S., Chen, M., … Zeng, H. (2023). *A high-resolution transcriptomic and spatial atlas of cell types in the whole mouse brain* (p. 2023.03.06.531121). bioRxiv. https://doi.org/10.1101/2023.03.06.531121

Yarnitzky, T., & Volk, T. (1995). Laminin Is Required for Heart, Somatic Muscles, and Gut Development in the Drosophila Embryo. *Developmental Biology*, *169*(2), 609–618. https://doi.org/10.1006/dbio.1995.1173

Yoo, S., Nair, S., Kim, H., Kim, Y., Lee, C., Lee, G., & Park, J. H. (2020). Knock-in mutations of scarecrow, a Drosophila homolog of mammalian Nkx2.1, reveal a novel function required for development of the optic lobe in Drosophila melanogaster. *Developmental Biology*, *461*(2), 145–159. https://doi.org/10.1016/j.ydbio.2020.02.008

Zhang, M., Eichhorn, S. W., Zingg, B., Yao, Z., Cotter, K., Zeng, H., Dong, H., & Zhuang, X. (2021). Spatially resolved cell atlas of the mouse primary motor cortex by MERFISH. *Nature*, *598*(7879), Article 7879. https://doi.org/10.1038/s41586-021-03705-x

Supplementary Figures

a

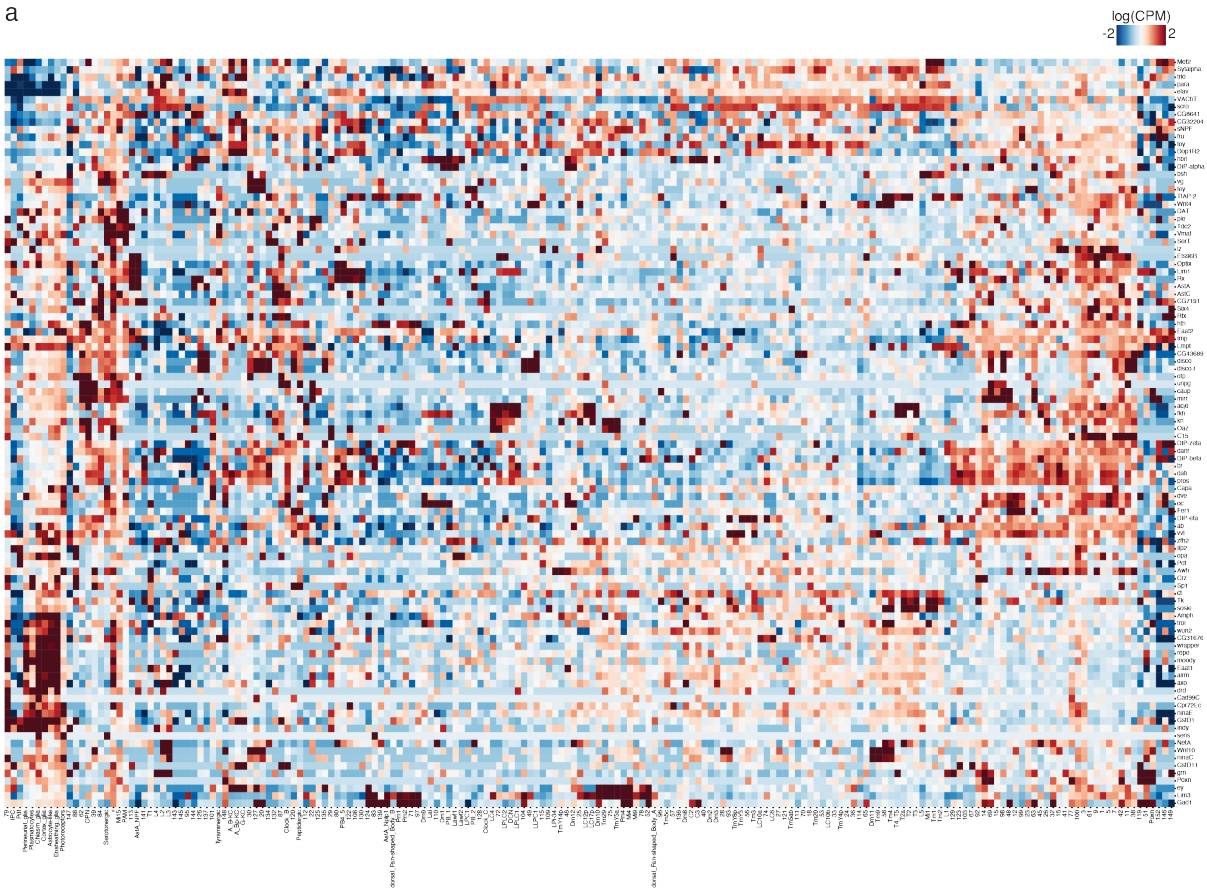

b

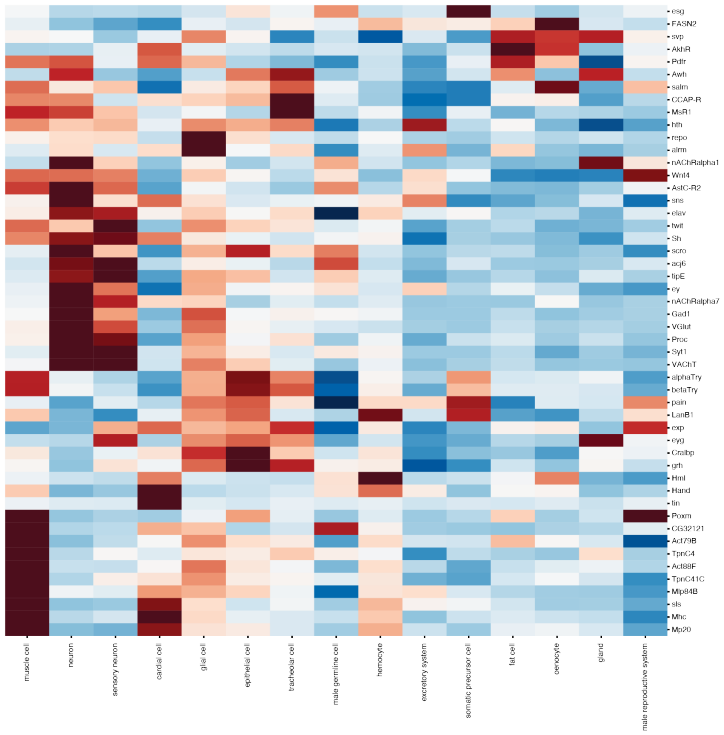

Fig. S1: Expression of FISH marker genes in single-cell datasets*. (a) Heatmap showing expression in standardized log(CPM) of 100 marker genes for single-cell clusters in the head dataset. (b) Heatmap showing expression in standardized log(CPM) of 50 marker genes for single-cell clusters in the FCA body dataset.*

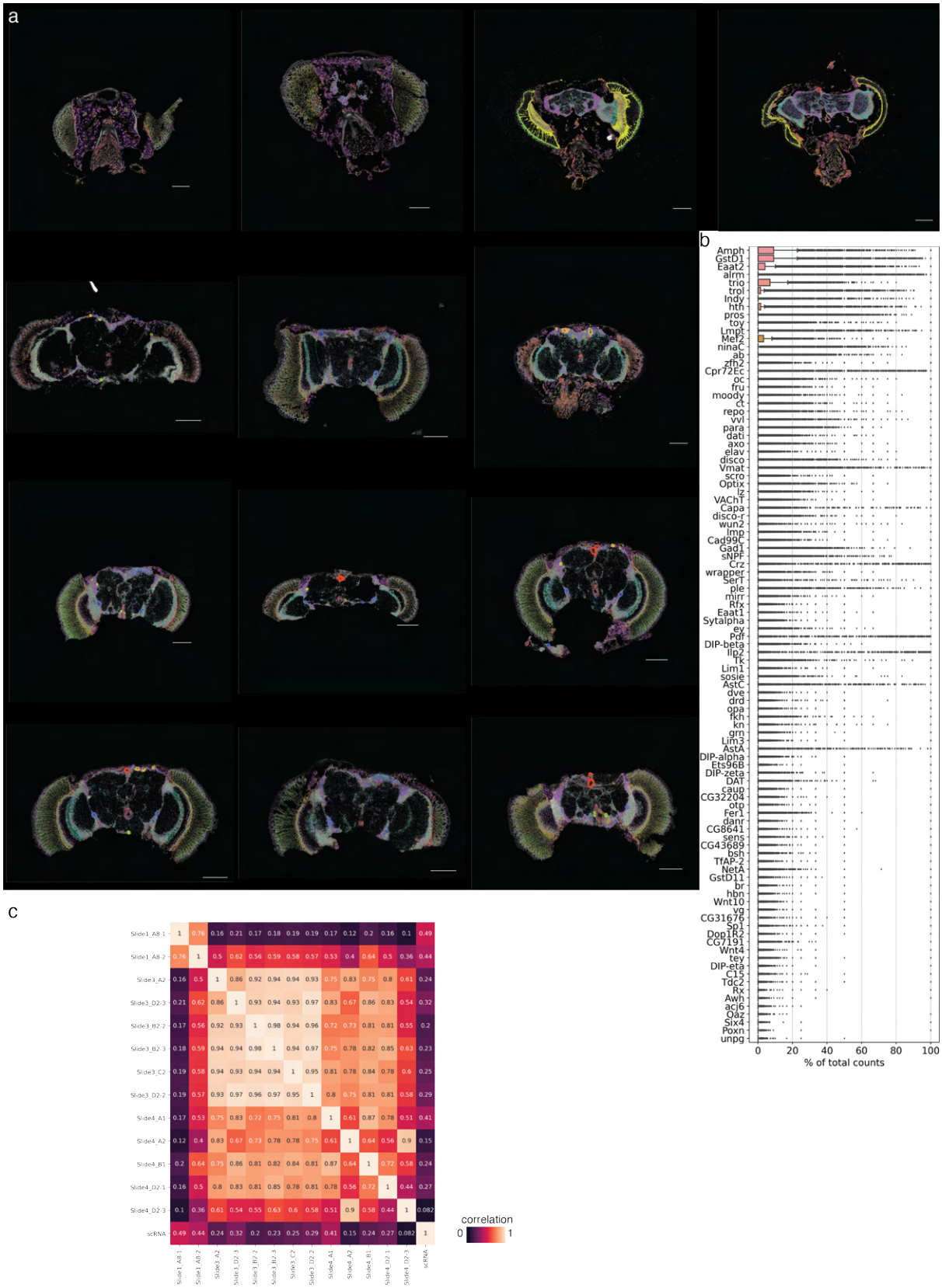

Figure S2: Head samples. *(a) All detected mRNA molecules color coded for all head samples used in analysis. Scale bars represent 100 µm. (b) Detected expression for each gene in all samples. (c) Heatmap showing Pearson correlation between samples.*

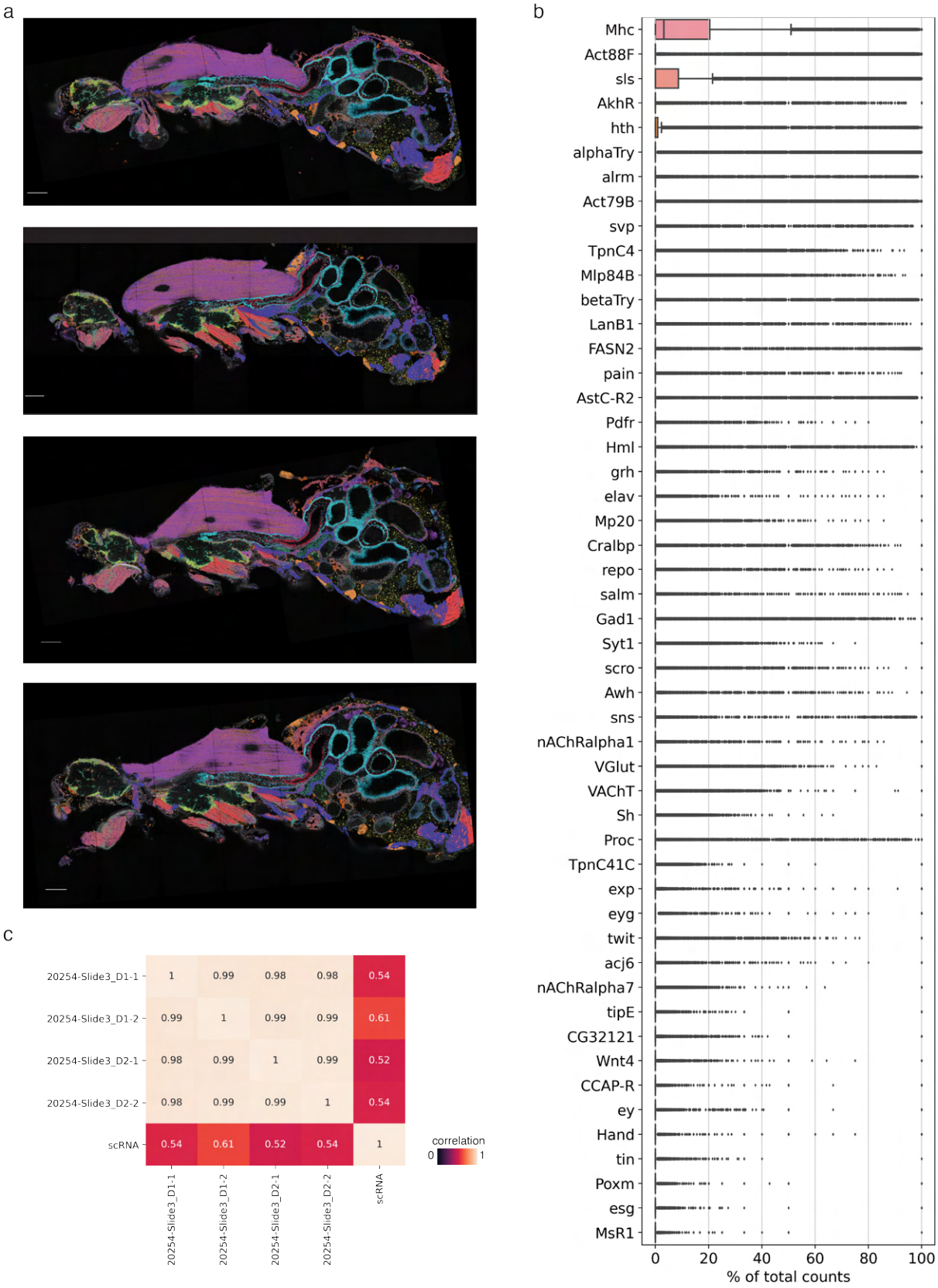

Figure S3: Body samples. *(a) All detected mRNA molecules color coded for all body samples used in analysis. Scale bars represent 100 µm. (b) Detected expression for each gene in all samples. (c) Heatmap showing Pearson correlation between samples.*

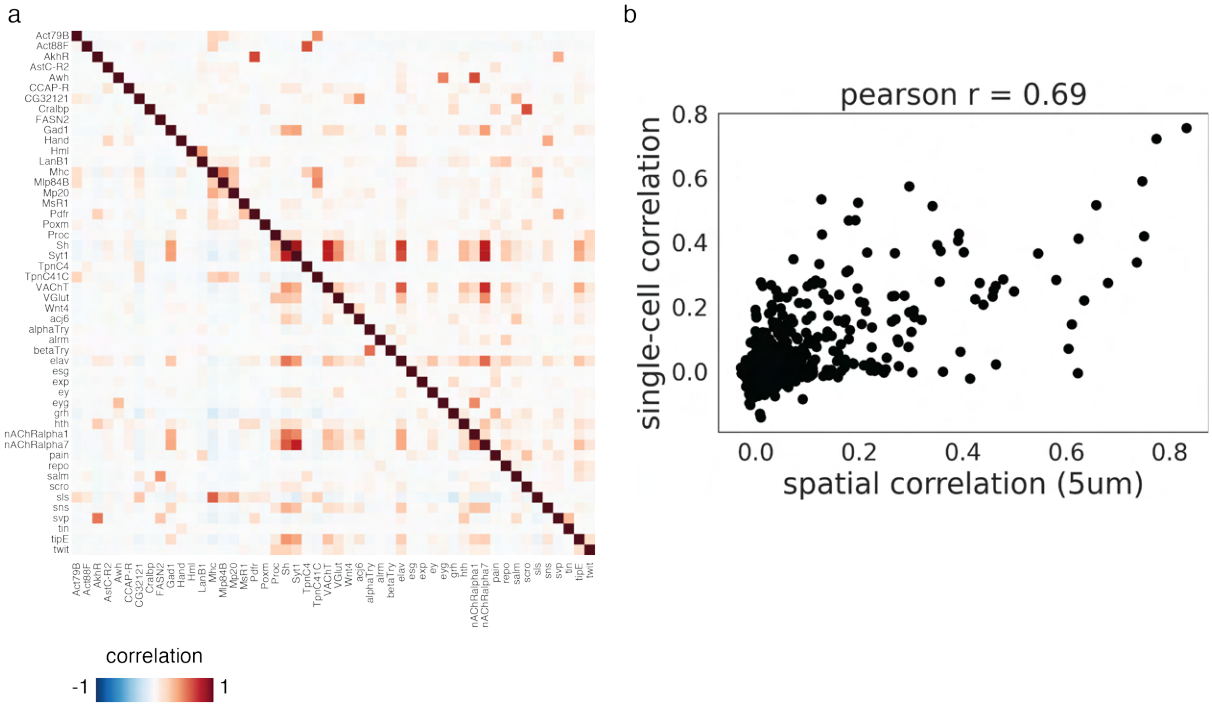

Figure S4: Comparison of body spatial datasets with body single-cell datasets. *(a) Composite heatmap showing gene-gene co-expression based on Pearson correlation. Bottom triangle calculated on spatial datasets (using grid-based 5 µm squares). Top triangle calculated using single-cells. (b) Gene-gene correlation measured across grid-based 5 µm squares and cells.*

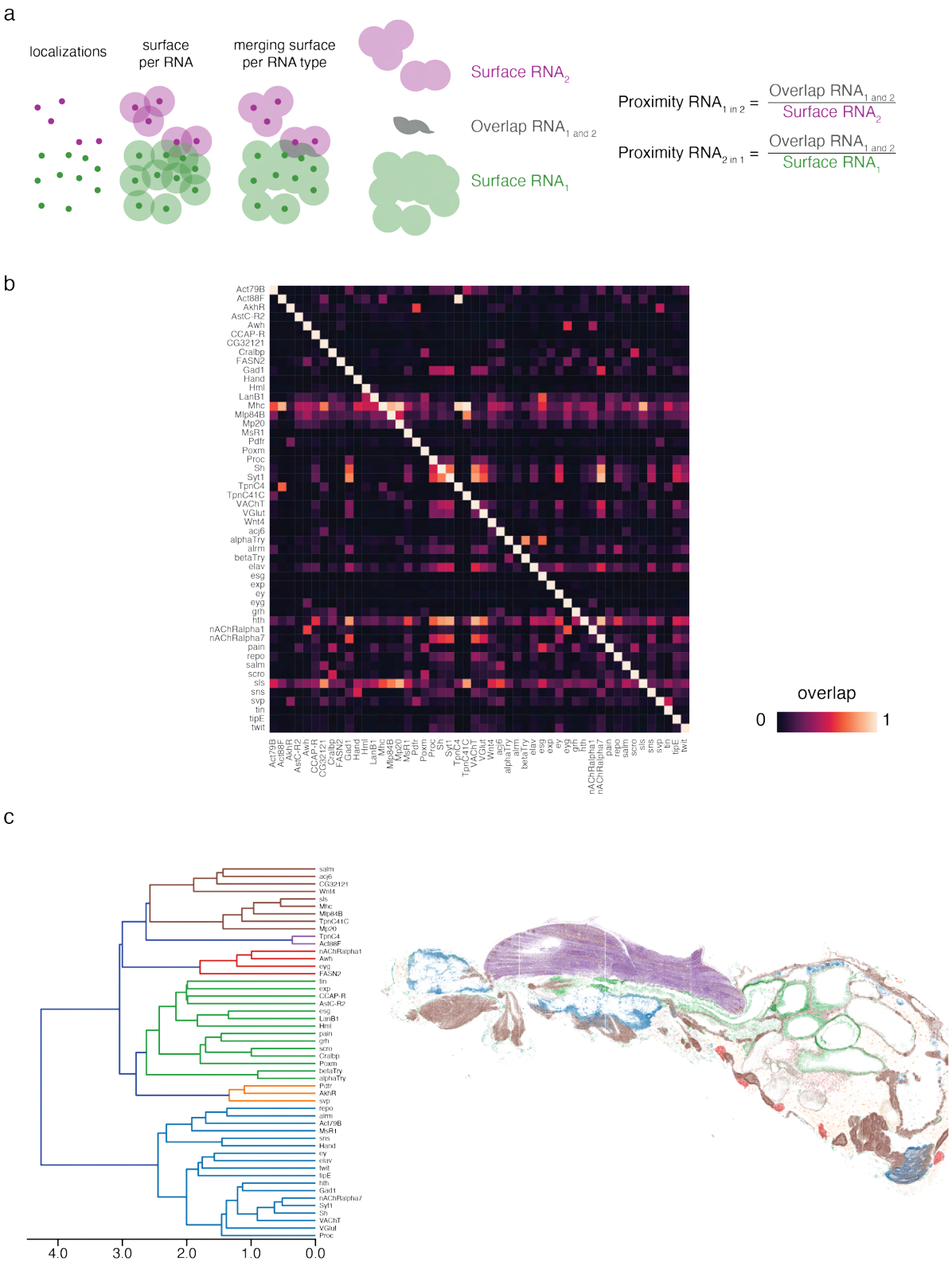

Figure S5: Comparison of head spatial datasets with brain single-cell datasets. *(a) Overview of colocalization algorithm. For each mRNA spot a disk of 4 µm diameter was used as search space. Overlaps in the disk area were then used to calculate proximity between genes. (b) Heatmap showing co-occurrence of genes with each other. (c) Ward's clustering of gene-gene proximities. (left) Dendrogram clustering of genes. (right) Spatial location of gene clusters.*

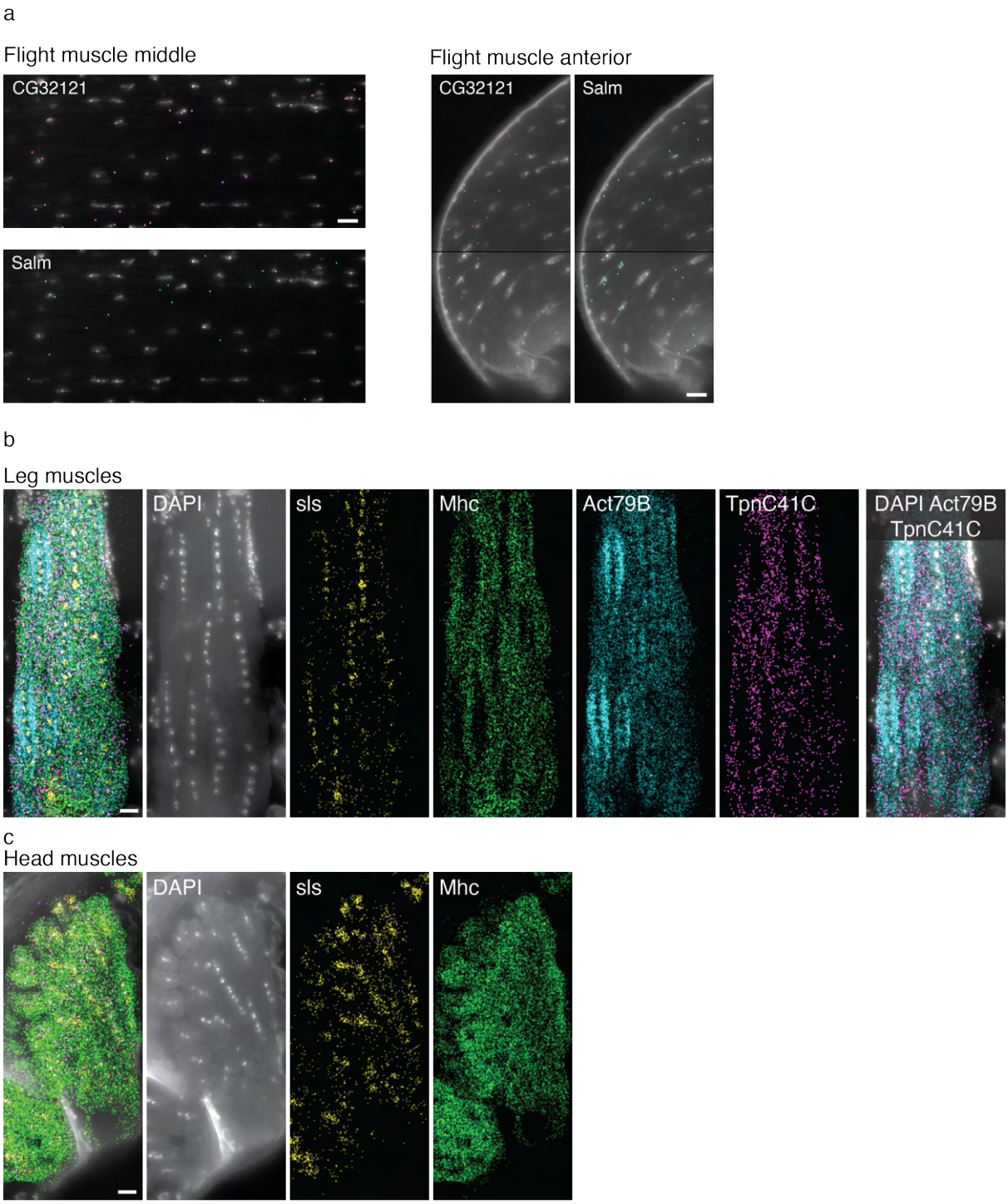

Figure S6: Subcellular mRNA localization in flight, leg and head muscles. *(a) Molecular Cartography of sparse genes CG32121 and Salm in flight muscles. (b) Molecular Cartography of genes following nuclei-enriched and* complementary striped bands*. (c) Molecular Cartography of sls and Mhc in head muscles, showing nuclei enrichment for sls. Scale bars represent 10 µm.*

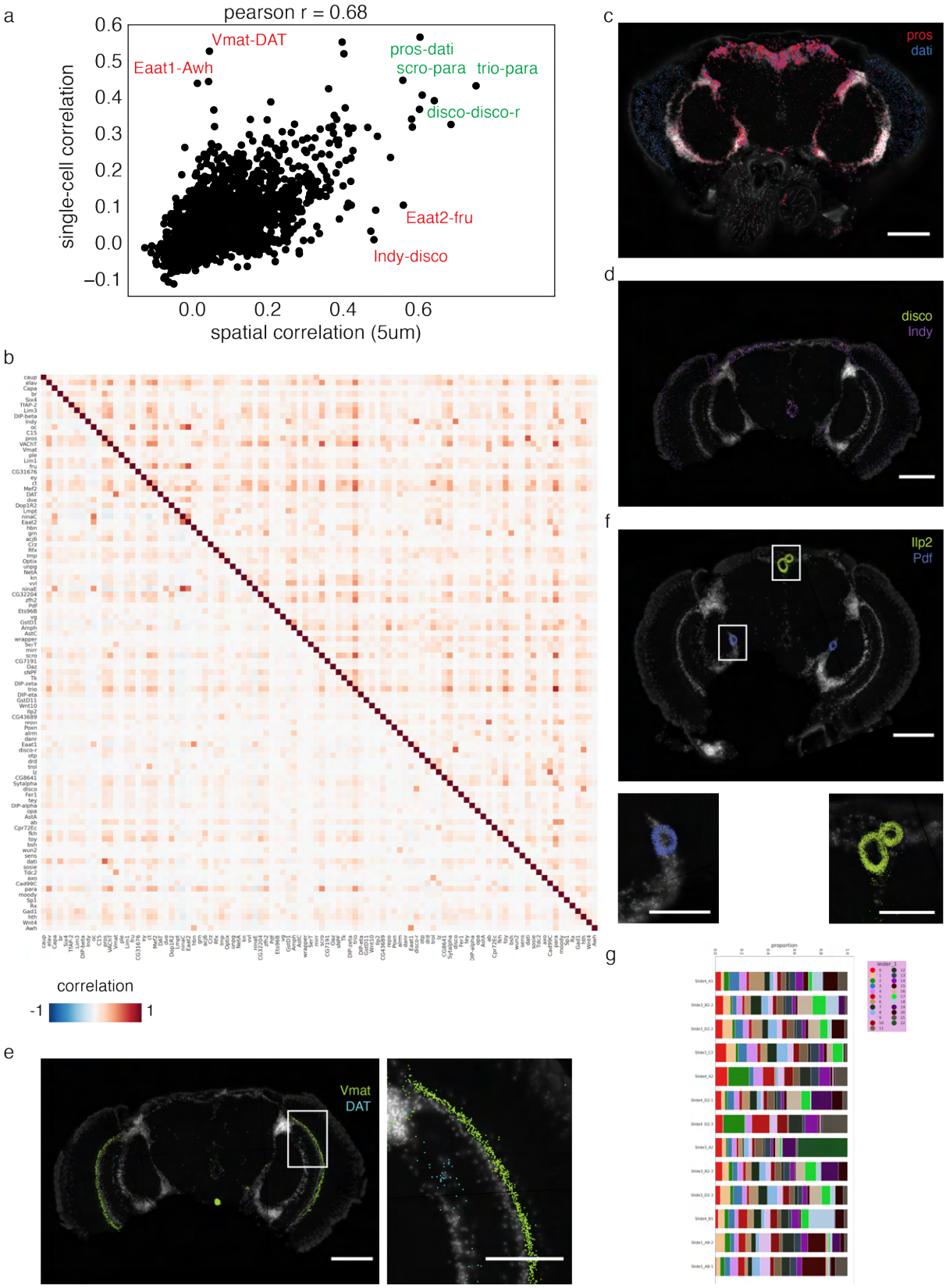

Figure S7: Comparison of head spatial datasets with brain single-cell datasets. *(a) Gene-gene correlation measured across grid-based 5 µm squares and cells. Mismatches shown in red, matching co-expression in green. (b) Composite heatmap showing gene-gene co-expression based on Pearson correlation. Bottom triangle calculated on spatial datasets (using grid-based 5 µm squares). Top triangle calculated using single-cell data. (c) Molecular*

Cartography showing high co-expression of pros and dati. Scale bar represents 100 µm. (d) Molecular Cartography showing co-expression of Indy and disco. Scale bar represents 100 µm. (e) Molecular Cartography showing expression of Vmat and DAT. Zoom shows non overlapping expression and expression of Vmat outside of nuclei marked by white DAPI signal. Scale bar represents 100 µm in the main image, 50 µm in zoom. (f) Molecular Cartography showing expression of neuropeptides Ilp2 and Pdf. Zooms show expression outside of nuclei marked by white DAPI signal. Scale bar represents 100 µm, 50 µm in zoom. (g) Stacked barplot showing sample composition based on Leiden 1 clustering.

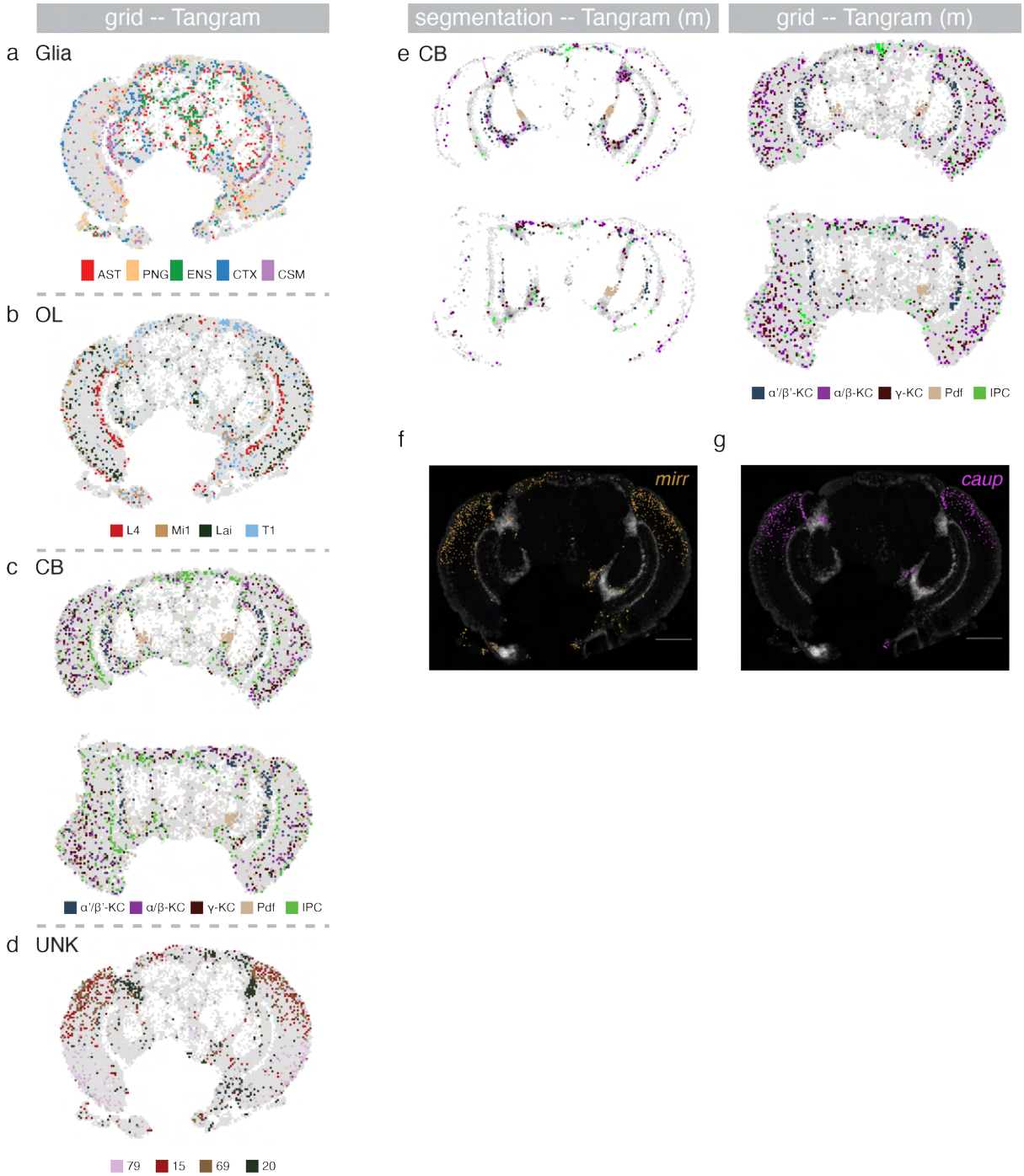

Figure S8. Results from Tangram on grid-based quantification*. a-d) Comparison of annotation of spatial data with single-cell RNA-seq. Grid-based squares are colored based on mapped single-cell cluster labels for (a) glia, (b) optic lobe, (c) central brain and (d) unknown clusters using Tangram. In (c) two brain slices are shown at different depths: central (top) and posterior (bottom). e) Effect of manually adjusted thresholds on Tangram score for nuclei segmentation (left) and grid-based quantification (right) for central brain clusters: 98%-quantile for assigning Pdf and 99%-quantile for IPC labels. f) Molecular Cartography showing expression of mirr. g) Molecular Cartography showing expression of caup. Scale bars represent 100 µm.*